Selective laser melting of Ti6Al4V-B_4C-BN *in situ* reactive composites

Kellen D. Traxel and Amit Bandyopadhyay*
W. M. Keck Biomedical Materials Research Laboratory
School of Mechanical and Materials Engineering
Washington State University, Pullman, WA 99164, USA
E-mail: amitband@wsu.edu

Abstract

An increasing desire for higher application temperatures and complex geometries for metallic materials has spurred significant development in additive manufacturing (AM) of metal-ceramic composites; however, limited process-microstructure-properties relationships exist for these materials and processing strategies. Herein we investigate the processing window and high-temperature oxidation performance of an *in situ* reactive, oxidation-resistant titanium metal-matrix composite reinforced with boron nitride (BN) and boron carbide (B_4C) via selective laser melting (SLM) to understand the effects of processing parameters on the *in situ* reactive characteristics and their effects on build reliability and high-temperature oxidation performance. SLM processing required a 50% decrease in overall energy density relative to titanium's optimal parameters to avoid processing failure due to the high *in situ* reactivity and exothermic reaction between feedstock materials. A precise balance was necessary to combine decreasing the input energy to avoid cracking due to *in situ* reactivity while simultaneously providing enough input energy to keep the bulk density as high as possible to limit porosity that contributes to processing inconsistencies at low input energy. Process optimization resulted in composites with as high as 98.3% relative density, comparable to some of the best composites reported in the literature, and high-temperature oxidation testing revealed a 39% decrease in oxidation mass gain compared to Ti6Al4V, owing directly to ceramic reinforcement. Our results indicate that control of SLM processing parameters can yield advanced composites with enhanced properties and characteristics compared to the base material, revealing an array of design possibilities for researchers and engineers in many fields.

Keywords: Selective laser melting; titanium; boron nitride; boron carbide; oxidation resistance.

1. Introduction

Demand for flexible manufacturing techniques to create advanced alloys and materials has led to the adoption of additive manufacturing (AM) in many industries to rapidly design, test, and evaluate new structures and materials quicker than traditional processing methods. One of these specific AM technologies, selective laser melting (SLM), has seen extensive use for high-value, single-material components with pre-existing alloys and materials but is increasingly desired for creating new materials and composites that can leverage the high cooling rates and resolution of powder bed based AM methods [1,2]. One variation of SLM that can create such materials involves modifying feedstock material composition to create multi-material,

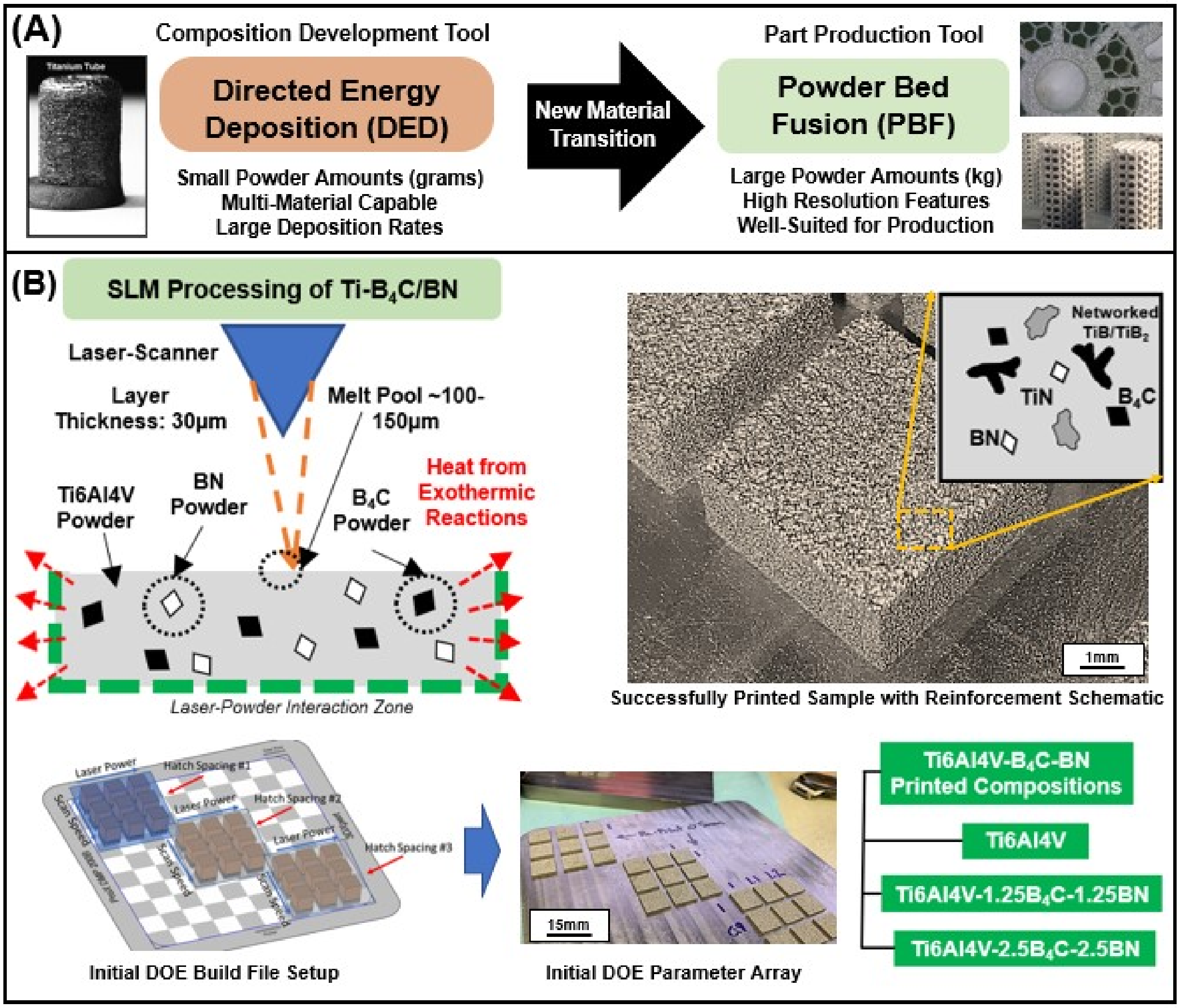

Figure 1: Metal-ceramic composite material development via laser-based AM **(A)** Workflow for using both DED and PBF based methods. Tubular image reproduced from ref. [10]. **(B)** Selective laser melting of reactive Ti6Al4V-B$_4$C-BN material system and the DOE setup for determining processing parameter range. Demonstration pieces designed and produced at the W.M. Keck Biomedical Materials Laboratory at WSU.

composite, and/or *in situ* alloys by leveraging high melt pool temperatures and/or *in situ* reactions among feedstock constituents [3]. Processing with these feedstocks results in composites with enhanced properties over the base material, with all the process-chain benefits of additive-based processing. This technique is highly promising for alloy systems like titanium, which suffer from low wear and oxidation resistance, and require alloying, coating, and/or reinforcement to meet the needs of specific applications, particularly in high-temperature oxidative environments [4]. Titanium's high reactivity at elevated temperatures can be exploited to form *in situ* reinforcing phases in the microstructure during additive-based processing in the presence of small amounts of ceramic, which can create refractory phases that are otherwise too expensive or impossible to produce using traditional methods. While promising, reactive-based SLM can pose processing challenges from exothermic reactions between feedstocks, resulting in hot-cracking and variability in processing success across materials systems and processing parameter sets [5]. Among many industries, these titanium-based composite materials can see applications in aerospace, nuclear, as well as biomedical, among others, due to their increased hardness, higher strength/weight ratio, better wear and oxidation resistance, and low density relative to other advanced or superalloy counterparts with similar refractory properties [6]. Among previous interesting work, Vrancken et al. (2019) investigated the reinforcement of Ti-Mo alloy with Mo_2C via the decomposition of the ceramic phase to produce reinforced TiC-microstructures in an SLM-based process, leading to high yield strength and hardness relative to the titanium matrix [7]. Xia et al. (2017) studied a Ti-B_4C system at various processing parameters, providing detailed analysis and imaging of the reaction zones forming between the ceramic and titanium matrix [8]. In related work, Kang et al. (2016) analyzed the wear performance of 2wt% reinforced titanium with CrB_2 for biomedical applications, looking primarily at the wear behavior regarding the processing parameters, citing lower coefficient of friction and wear rates in comparison to the base material with the addition of ceramic [9]. These works highlight some examples of how SLM can produce *in situ* titanium metal-matrix composites with improved properties over titanium and its alloys alone.

Like metal-based alloy development, however, metal-ceramic composites require an in-depth understanding of the processing parameter-composition-properties relationships to manufacture reliable parts for end-use applications. A significant knowledge gap exists in these material systems due to the minimal information related to general composition-processing parameter-property relationships (particularly for AM-based processes), which significantly hinders widespread adoption of the processing technology. Additionally, the large relative amount of feedstock material required to investigate new materials using selective laser melting (several kilograms) makes initial composite material development expensive and very high-risk, deterring advances in development (see **Fig. 1A**). This motivates the investigation of combining both laser-based methods, namely, SLM and powder-flow-based AM, i.e., directed-energy-deposition (DED), owing to the minimal amount of material required (several grams) in DED-based processing. While DED and SLM are not equivalent in terms of capabilities and resolutions, DED systems typically maintain multiple feedstock hoppers capable of printing multiple compositions side-by-side via laser; however, its feature resolution (~200-300μm layer thickness) does not allow for the fine features that are required for advanced applications (SLM layer thickness ~30-50μm). Because DED uses a laser, however, laser-material interactions occurring during DED processing should represent that exhibited in SLM-based processing and could make a desirable small-scale development tool for understanding processing-properties relationships before transitioning a specific composition to SLM, which requires a more significant investment of material and resources.

Along this same line of reasoning, our preliminary work using DED-based processing investigated a 5wt% total ceramic reinforcement of B_4C/BN particles that resulted in a unique TiB/TiB/TiN reinforcing microstructure with improved hardness, strength, and oxidation resistance in comparison to the titanium matrix [10]. Our other work using DED produced similarly reinforced microstructures in titanium, zirconium, and titanium-zirconium systems with improved wear and oxidation characteristics as well [5,11,12]. These works demonstrated that the specific Ti-B_4C-BN precursor composite material system and resulting microstructures could be processed using a laser-based AM method to create materials with improved properties, requiring only grams of material to investigate via DED. To fully leverage this composition's benefits, however, it was hypothesized that the same system could be processed using SLM to fully leverage the high-resolution capability and production value for component end-use and demonstrate a novel DED-SLM workflow that can be exploited by manufacturers that envision keeping material and/or alloy development in-house. This has not been attempted for a metal-ceramic composite system in the literature to the best of the authors' knowledge. The titanium-based composite material system of interest in the current study is highly exothermic (see **Fig. 1B**), meaning that non-trivial modifications to titanium processing alone will be necessary to achieve high density and quality components using this method, and processing success in DED may not directly translate to the SLM system. Further, it was envisioned that variation of input processing parameters would play a vital role in the resulting processability, microstructure, and eventual oxidation performance at high temperature, motivating detailed investigation. To this end, titanium-boron carbide-boron nitride composites were manufactured using SLM in the present study by premixing Ti6Al4V powder and B_4C/BN in a similar reinforcement amount from our previous work in ref. [10], i.e., Ti6Al4V-2.5wt%B_4C-2.5wt%BN and Ti6Al4V-1.25wt%B_4C-1.25wt%BN at variable processing parameters (laser power, scanning speed, hatch spacing). These specific compositions were chosen due to previous success during DED-based processing (5wt% overall reinforcement) [10] and 2.5wt% overall reinforcement to see the influence of overall ceramic reinforcement. Extensive microstructural evaluation via scanning electron microscopy (SEM), Vickers microhardness, and relative density measurements were performed to understand the *in situ* reactivity at variable processing conditions and composition and the formation of defects and processing-induced cracking at various input parameters. This work's key novelty lies in processing a previously DED-designed composition via SLM, indicating the ability to combine both main laser-based AM methods for designing, testing, and producing advanced composite materials at reduced cost and complexity for manufacturers. Our results aid in understanding composition-processing parameter-properties relationships for novel AM-produced materials, reducing the barrier to entry for end users in many different industries and advanced application spaces.

2. Materials and methods

2.1 Processing via selective laser melting and parameter development methodology: Our selective laser melting system (3DSystems DMP Pro 200) operates a 300W fiber laser with scanning speeds capable of 2400 mm/s, and layer thickness held constant at 30μm for all prints. An extensive review of this process and mechanics are discussed in ref. [13]. The powder spreader maintains a counter-rotating hard-recoater that spreads powder as it initially makes the first pass over the previously sintered layer and subsequently compacts on the way back to the powder feed bin, as shown schematically in **Fig. 1**. All prints were performed in an enclosed argon environment at under 30°C and < 500ppm O_2 to limit oxidation on each layer. Powder feedstock included "virgin" Ti G. 23 (LaserForm® Ti6Al4V ELI, Gr. 23) in the particle size range of 5-25μm (evaluated via SEM), non-spherical-B_4C powder (Presi, Switzerland), and non-spherical hexagonal-BN powder ("PTX60" from Momentive Performance Materials, Waterford, NY) both sieved to under 65µm before premixing and entrance to the build chamber, as recommended from the system manufacturer. A Ti-Gr. 2 plate of ~1/2" thickness was utilized as a build substrate (purchased from Onlinemetals.com). As previously developed via directed energy deposition, titanium-boron carbide-boron nitride compositions of Ti6Al4V-2.5wt%B_4C-2.5wt%BN (henceforth, Ti6Al4V-2.5B_4C-2.5BN) and an additional Ti6Al4V-1.25wt%B_4C-1.25wt%BN (henceforth Ti6Al4V-1.25B_4C-1.25BN) were premixed via ball-milling (without milling media) for 45mins before entering the build chamber. The Ti6Al4V-1.25B_4C-1.25BN composition was processed via the Ti6Al4V-2.5B_4C-2.5BN powder mixture with added Ti6Al4V/B_4C/BN to achieve the correct composition. Between each print and before mixing the Ti6Al4V-1.25B_4C-1.25BN composition, the powder was re-sieved to under 65µm to ensure processability with the system, as per manufacturer recommendation. It is noted here that the Ti6Al4V-1.25B_4C-1.25BN composition's processing parameter range was determined based on knowledge of the processability of the higher reinforcement amount composition, so the same processing parameters were not used for both compositions but were within a similar energy density range. The driving parameter for this study is the input energy density to the material, which is directly related (in this case) to the laser power P, scanning speed v, hatch spacing h, and layer thickness t, as such [14]:

$$Energy\ Density = \frac{P}{thv}$$

The initial 10mm square sample prints were performed centering around standard Ti6Al4V parameters (63.0Jmm^{-3}), with 5-10% adjustments in scanning speed, laser power, and hatch spacing as shown in **Figs. 1B & 2,** where 27 individual parameter sets were tested with variations in parameters, and subsequently, variable processability was observed. Initial samples were printed at only 5mm height to conserve powder while finding an optimal processing range with the final goal of printing 10mm tall samples. Some initial samples printed at more than ~50 Jmm^{-3} had to be stopped mid-print due to failure and debonding from the build substrate (as shown in the bottom left image of **Fig. 2**). In these situations, the build was paused for under 5mins to change the build file where the remaining successful samples could be completed printing towards their 5mm final height to ensure that build bed temperatures were maintained for the remaining samples. Candidate parameter sets that were successful at 5mm build height were transitioned to builds at 10mm height to understand processability further. The overall process parameter range is shown in **Fig. 3** for both the Ti6Al4V-2.5B_4C-2.5BN and Ti6Al4V-1.25B_4C-1.25BN compositions, where designations of outer visible surface quality such as "Crack-Free" indicates minimal observable surface cracking and full processability throughout the entire print, "Minor-Cracking" indicates visible surface cracking and the potential for out-of-plane distortion and build failure, and "Full-Cracking" indicates extensive surface cracking and/or debonding from the substrate or previously fused layers and complete failure of the sample to finish printing throughout the entire build sequence. After a build sequence was finished, samples were removed via band-saw cutter, and the plate resurfaced to be used again on the next batch of processing parameters.

Table 1: Processing parameters successful at 5mm tall blocks chosen for further study into 10mm block samples in the current study. See supplemental information for all process parameters attempted.

Composition	**Layer Thickness (µm)**	**Laser Power (W)**	**Hatch Speed (mm/s)**	**Hatch Spacing (µm)**	**Energy Density (Jmm^{-3})**
Ti6Al4V	30	180	1600	60	63.0
Ti6Al4V-2.5B_4C-2.5BN	30	137	2070	70	31.5
		123	1980	60	34.5
		130	2070	50	41.9
Ti6Al4V-1.25B_4C-1.25BN	30	113	2505	70	21.5
		103	2070	70	23.7
		95	2505	50	25.3

*Note Ti6Al4V parameters optimized for >99.5% relative density as-processed.

2.2 Metallographic preparation, density, and phase analysis: Several samples from both compositions were sectioned via diamond saw, cold-mounted in acrylic resin, and ground using 80-2000 grit SiC paper, followed by polishing via alumina suspension on a polishing pad from 1µ down to 0.05µ. X-Ray Diffraction (XRD) (X'Pert PRO PANalytical, Almelo, Netherlands, Cu Kα source and a Ni filter) was performed for a Ti6Al4V printed sample as well as a Ti6Al4V-2.5B_4C-2.5BN sample printed at 41.9Jmm^{-3}, with intensities normalized by the highest-count peak in each composition. Relative density was evaluated using the standard Archimedes method, with the composites' theoretical compositions used as the standard for achieving 100%

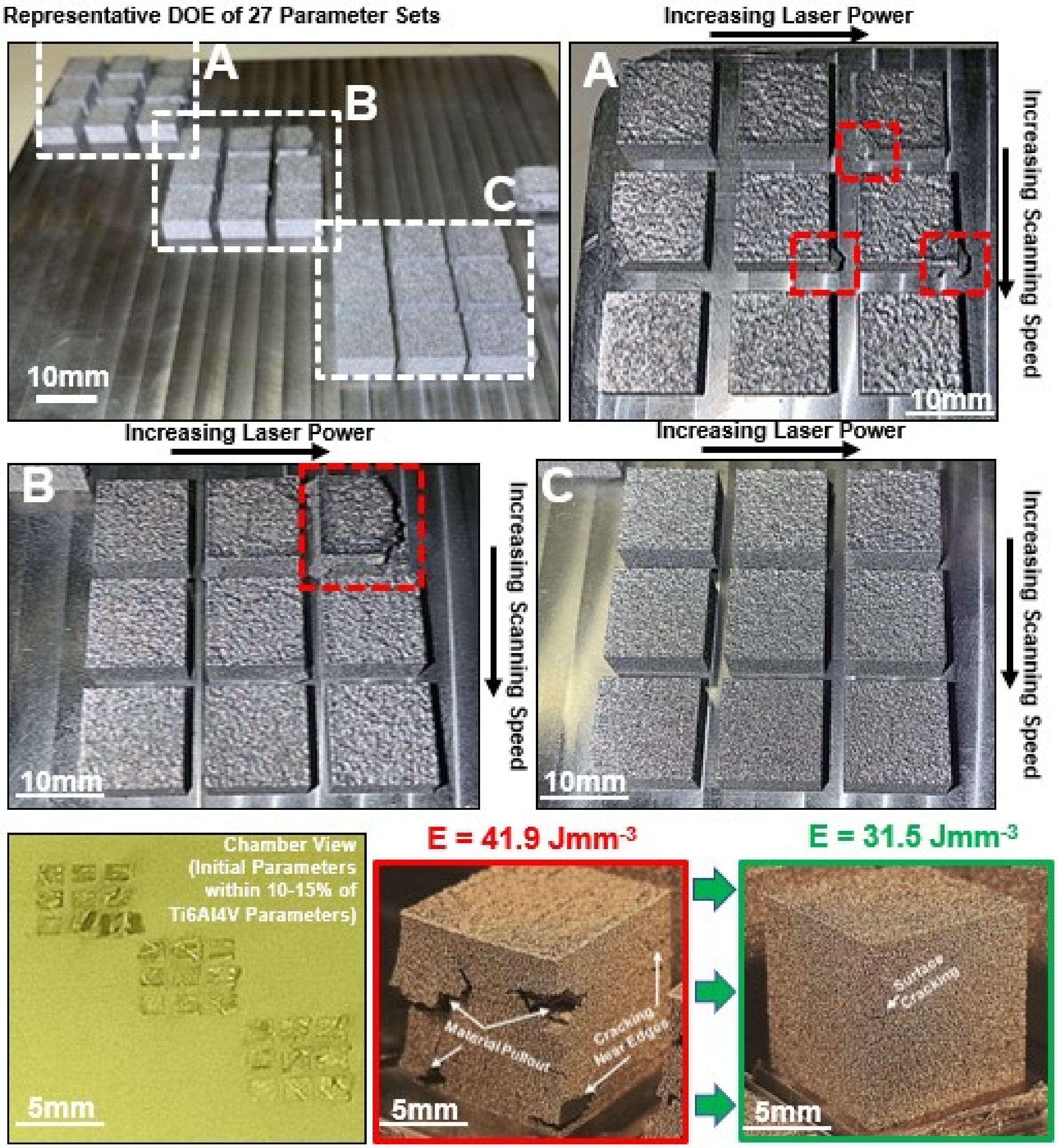

Figure 2: Comparison of processability of initial Ti6Al4V-2.5B_4C-2.5BN results to final 3 parameter sets used in study.

relative density. Three individual samples were used for each treatment's measurements (i.e., different processing parameter sets and/or composition). Vickers cross-section hardness indents (Phase II, Upper Saddle River, NJ) were taken in line with ASTM standards for both metals and advanced ceramics on the polished (unetched) samples in the as-processed conditions [15,16]. 5-8 indents were used at each of the reported values (parameter set, composition, location within the build height of the sample). High-magnification microstructural imaging, Field-Emission Scanning Electron Microscopy (FESEM, or SEM) was utilized on etched samples. Etching was performed via submersion for 10s in Kroll's Reagent (92mL DI Water, 6mL HNO_3, & 2mL HF).

2.3 Isothermal thermogravimetric analysis (TGA): For isothermal oxidation testing, mass increase measurement on 3mm samples cut from the as-printed structures was performed via Netsch STA 409-PC Luxx (Burlington, MA). The optimal processing parameter sets were used for each composition (31.5 Jmm^{-3} for the Ti6Al4V-2.5B_4C-2.5BN composition, 21.5 Jmm^{-3} for the Ti6Al4V-1.25B_4C-1.25BN composition, and the standard processing parameters for Ti6Al4V). Two individual samples from each composition and control (AM-produced Ti6Al4V) were ground with 80-grit SiC paper and cut into 3mm cubes for testing at 700°C for 25 and 50 hours. For testing, an alumina crucible held each sample, which was all weighed before testing and throughout the entirety of each test (accuracy of 0.01mg). An airstream of ~0.5 psig and flow rate of 40 mL/min, with a filter, was used to keep the moisture content consistent. An initial heating rate of 20 °C/min was used until 850 °C, withholding for 25h and 50h, followed by a 40 °C/min cooling rate down to 20 °C. As-printed microstructures, as-oxidized scale, and cross-sections were each analyzed using SEM imaging. High-mag imaging was performed via Field-Emission Scanning Electron Microscopy (FESEM, SEM) on etched as-printed as well as as-oxidized specimens (submersion for 20s in Kroll's Reagent (46mL DI Water, 3mL HNO3, & 1mL HF).

3. Results

After carefully adjusting processing parameters, titanium matrix composites with both 2.5wt% and 5wt% overall reinforcement were successfully manufactured using selective laser melting technology. The process leverages high-temperature reactions during printing that result *in situ* reinforcing phases. High magnification imaging and analysis were utilized to understand the resulting microstructures, phase formation, and processing-induced defects that lead to limited processability ranges for these composite materials, aiming to understand how to tailor processing parameters for reliable manufacturing to transition composite compositions from DED-based AM to powder-bed based AM.

3.1 Reactive-processing parameter development: Parameter selection played a significant role in the processability of the composite compositions. Both compositions were printed with an "island" scanning strategy for every combination of parameters that divides each cross-section into hexagonal-hatching shapes (6mm in size) that are then filled in at the user-defined scanning parameters to limit heat buildup. Additionally, contour scans were eliminated to reduce any influence on the processability apart from the main "bulk" hatching parameters. A characteristic design of experiment (DOE) build for the Ti6Al4V-2.5B_4C-2.5BN composition is shown in **Fig. 2**. Three parameters (laser power, scanning speed, hatch spacing) were varied to understand the effect of input energy density on the resulting processability of the composites. In this case, Section A (9 different parameters) was of the same hatch spacing (50µm) and showed significant sample debonding at the higher laser power/lower scanning speed combinations. For the higher hatch spacing in Section B (59.5µm, lower energy density), processing failure was only found at the highest energy density combination, and all samples were processable at 5mm height for the largest hatch spacing in Section C (70µm). **Fig. 2** also shows the inside of the chamber (bottom left image) for an initial print that was centered near Ti6Al4V's processing parameters (63.0 Jmm^{-3}) showing the distortion and debonding that occurs with the presence of the ceramic reinforcement for nearly every parameter set. After this initial build, it was evident that lowering the input energy density would be essential for producing high-quality samples. Further, the camera images show the difference in the processability of 10mm tall samples produced at 31.5 Jmm^{-3} and 41.9 Jmm^{-3}, indicating how much of an impact a ~33% increase in energy density can have on the processability of samples up to 10mm height. Further, **Fig. 3** and **Supplemental Tables 1 & 2** show all parameter sets and processing outcomes for samples produced at 5mm height.

Input energy density, as a derived parameter, plays a significant role in the processability of the composite compositions (see **Fig. 2**). Planes of constant energy density (20-65Jmm^{-3}) at 30µm layer thickness are shown across various parameters to compare the actual parameters used to the theoretical energy densities (see **Fig. 3**). It is important to note that the designations defined here as "Crack-Free," "Minor Cracking," and "Full Cracking" are qualitative and describe the visual look of the samples either during or post-processing, without regard for any internal defects or cracking present in the samples which were also found after cross-sectioning the samples, and some samples may verge on the boundary of being Minor/Full/Crack-Free in some cases. For the Ti6Al4V-2.5B$_4$C-2.5BN composition, no parameter combination was able to be processed Crack-Free above ~40Jmm^{-3}, with an exception being the sample produced at a laser power of 130W, scanning speed of 2070 mm/s, and hatch spacing of 50µm, which subsequently exhibited Full-Cracking characteristics for 10mm tall samples (see **Fig. 2**). Most Crack-Free samples for the Ti6Al4V-2.5B$_4$C-2.5BN composition were processed successfully at the higher hatch-spacing of 70µm, as well as lower laser powers and higher scanning speeds indicated by the green "Crack-Free" green dots. A transition from Crack-Free to Minor-Cracking occurs most nearly around ~45-50Jmm^{-3}. Most samples above that move towards Ti6Al4V's

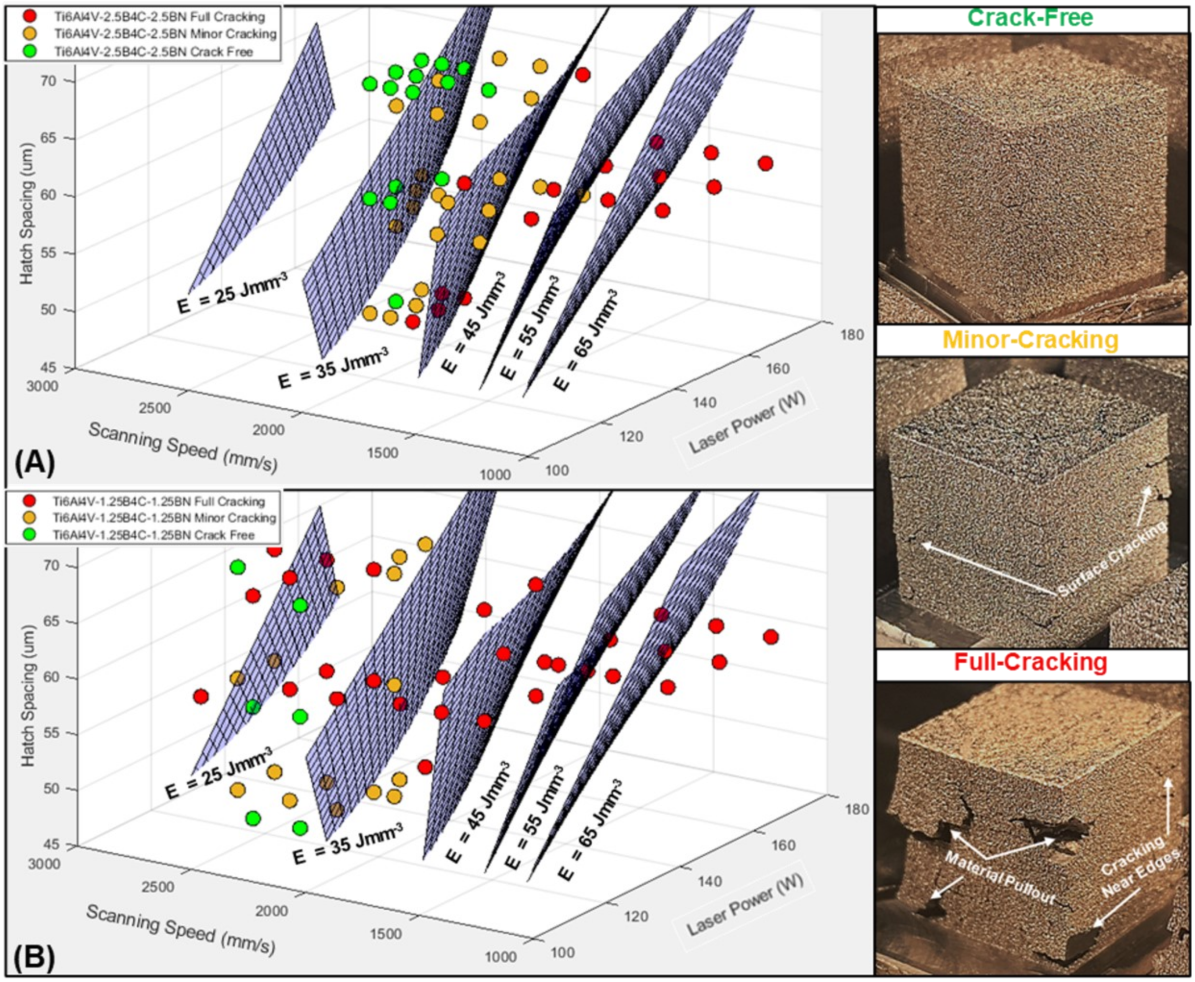

Figure 3: Processing parameter space comparison for each composition considering processability without failure. **(A)** Ti6Al4V-2.5B$_4$C-2.5BN**. (B)** Ti6Al4V-1.25B4C-1.25BN. Inset images of variable-processing success samples are from the Ti6Al4V-2.5B$_4$C-2.5BN composition. "Minor-Cracking" indicates visible surface cracking and the potential for out-of-plane distortion and build failure, and "Full-Cracking" indicates extensive surface cracking and/or debonding from the substrate or previously fused layers and complete failure of the sample to finish printing throughout the entire build sequence.

energy input of 63Jmm^{-3} were unsuccessful and caused build failure during processing. Minor-Cracking samples were mainly characterized by surface cracks that do not cause build failure (and can be built higher) but are unsuitable for reliable manufacturing or end-use applications. Full-Cracking samples were mainly characterized by material pullout on the surface in addition to cracking and/or debonding from the substrate. Often, these two designations had parameter sets that may have fallen into both categories but produced samples with poor surface characteristics. The Ti6Al4V-1.25B$_4$C-1.25BN composition interestingly exhibited a similar processing range to the Ti6Al4V-2.5B$_4$C-2.5BN composition, with success shifted even further below ~35Jmm^{-3} for Crack-Free designation, despite having an overall lower wt% of ceramic reinforcement. In comparison to the Ti6Al4V-2.5B$_4$C-2.5BN composition, the Ti6Al4V-1.25B$_4$C-1.25BN composition had successful Crack-Free parameters at each of the tested hatch spacings as opposed to mainly the larger 70µm, and a quicker transition from Crack-Free parameters to the Minor Cracking/Full-Cracking range, indicating a more scattered degree of processability concerning the overall energy density changes. More specifically, samples that exhibited processing failure or minor cracking were both present very near the processing range for crack-free (~20-25Jmm^{-3}), indicating an almost immediate transition to parameters that were not reliably processable from the successfully processable range, despite having a lower overall ceramic reinforcement amount. Three candidate processing parameter sets from each composition that was the most consistent and visually successful at 5mm height (see **Table** 1) were chosen for processing up to 10mm tall blocks, namely 31.5 Jmm^{-3}, 34.5 Jmm^{-3}, 41.9 Jmm^{-3} for the Ti6Al4V-2.5B$_4$C-2.5BN composition, and 21.5 Jmm^{-3}, 23.7 Jmm^{-3}, 25.3 Jmm^{-3} for the Ti6Al4V-1.25B$_4$C-1.25BN composition (see **Table 1**).

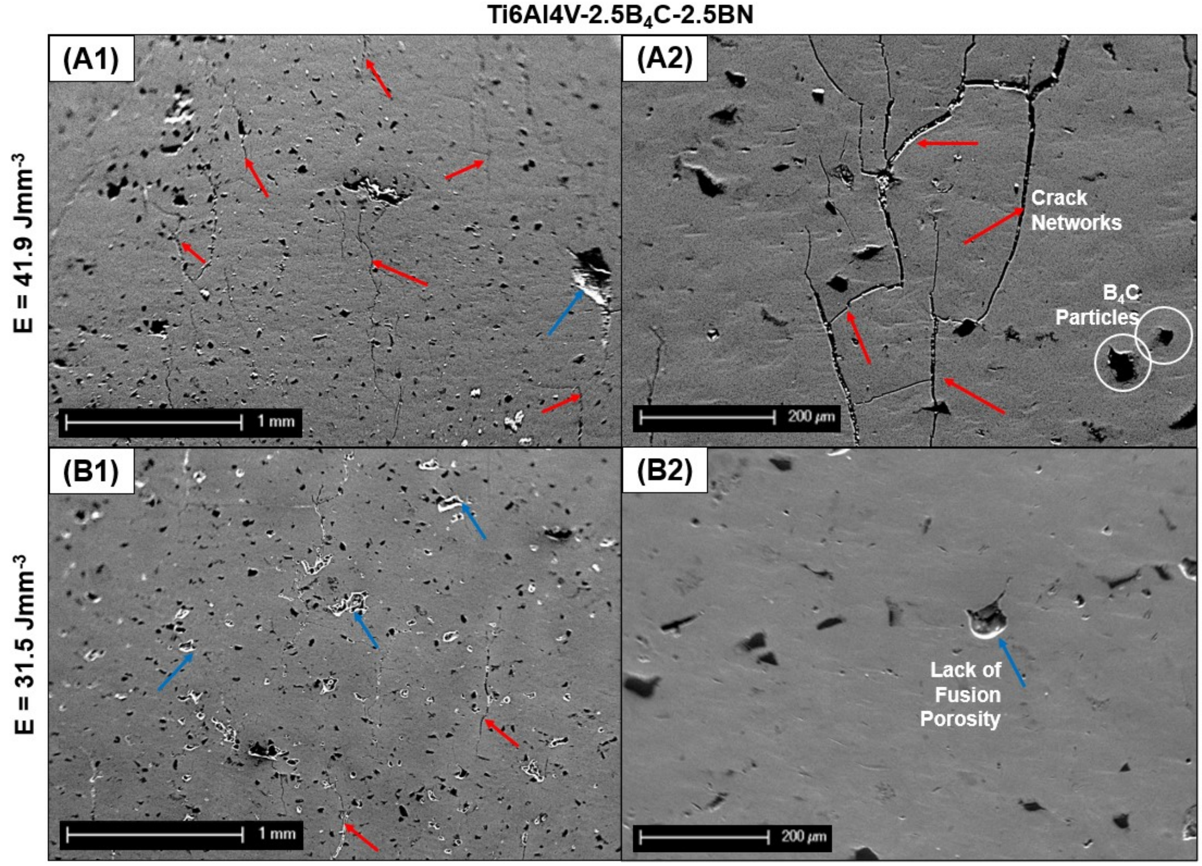

Figure 4: Comparison of low-mag microstructures at different input energy densities for the Ti6Al4V-2.5B_4C-2.5BN composition. Red arrows indicate crack formation in microstructures and blue arrows indicate lack of fusion (LOF) porosity. Build direction is vertical.

3.2 Microstructure, hardness, relative density, and phase analysis: Cross-sectional microstructures heavily depended on the processing parameters and input energy density for both compositions. Cross-sections of Ti6Al4V-2.5B_4C-2.5BN processed at both 41.9Jmm^{-3} and 31.5Jmm^{-3} are shown in **Figs. 4A1 & 4A2**, as well as **Figs. 4B1 & 4B2**, respectively. Homogenous distribution of B_4C particles was observed for all compositions, indicating a uniform mixture and spread of powder over the build surface from layer-to-layer. For the

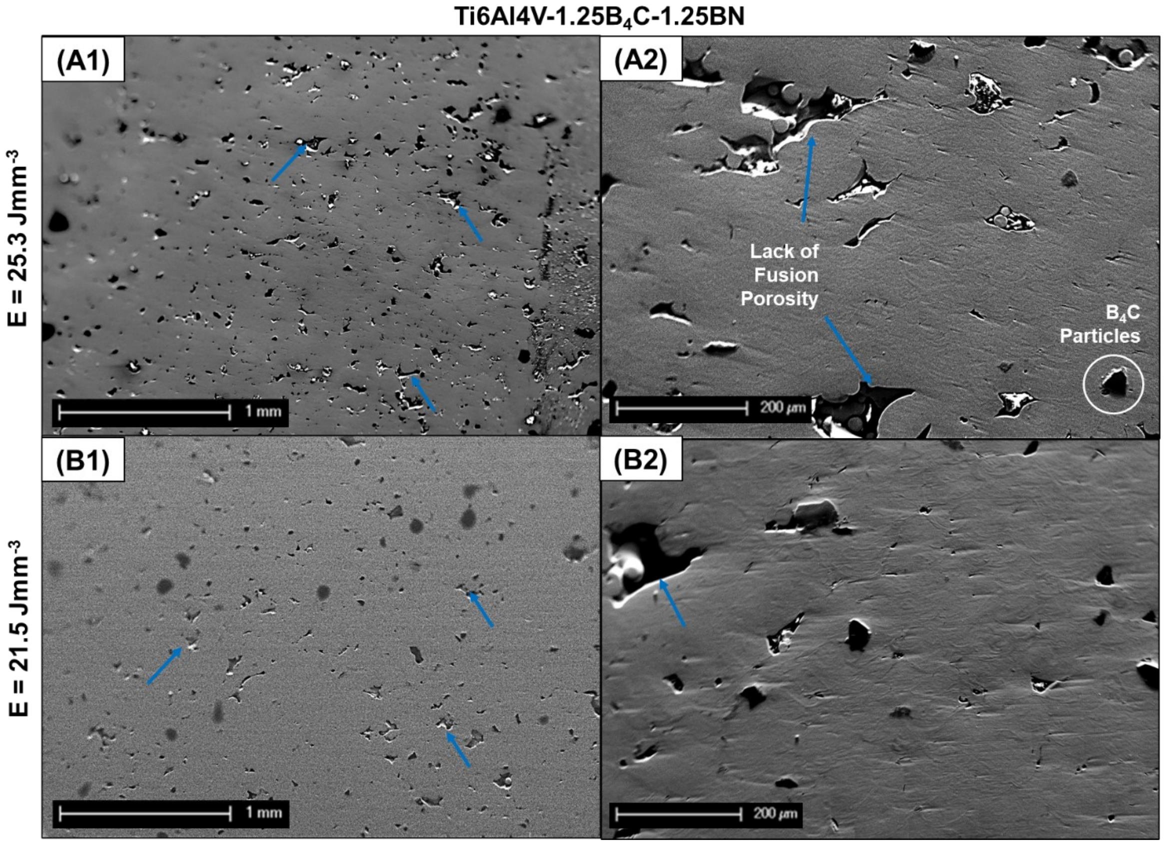

Figure 5: Comparison of low-mag microstructures at different input energy densities for the Ti6Al4V-1.25B_4C-1.25BN composition. Arrows indicate lack of fusion in microstructures. Build direction is vertical.

Ti6Al4V-2.5B_4C-2.5BN sample produced at 41.9Jmm^{-3}, vertical cracks (see **Fig. 4A1**) extending ~1mm were present in the microstructure (red arrows), as well as some minor lack of fusion porosity (blue arrow). Upon closer examination (**Fig. 4A2**), the crack networks in the microstructure tended to be connected via B_4C particles in the microstructure and were mostly present at the

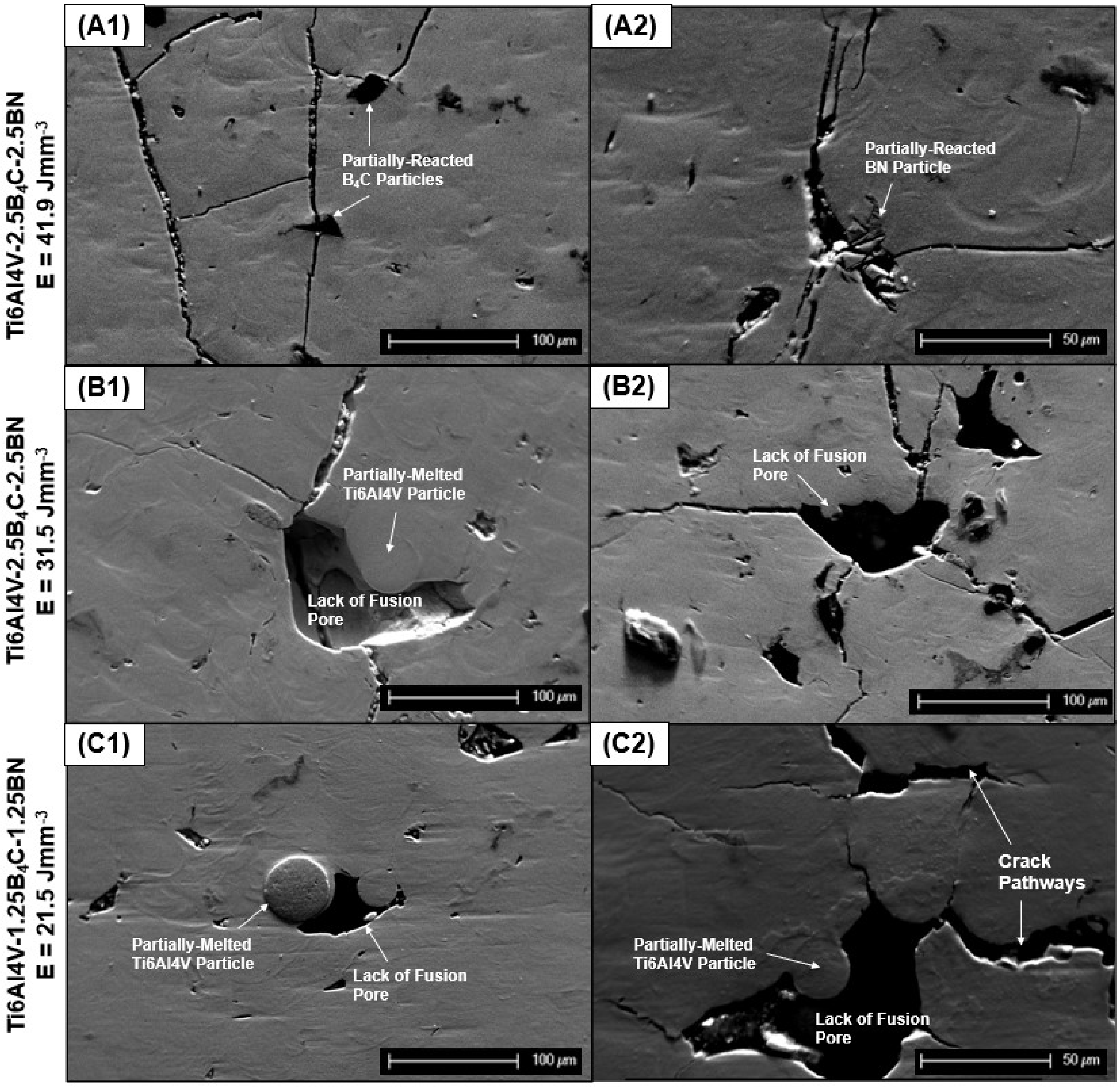

Figure 6: Representative cracking and defects in each of the compositions. Build direction is vertical.

edge of the sample as opposed to the bulk material, indicating some geometric challenges of creating sharp edge features with this composition. Comparatively, the Ti6Al4V-2.5B_4C-2.5BN composition produced at 31.5Jmm^{-3} exhibited small vertical cracks (see **Fig. 4B1**) extending < 0.25mm in the microstructure (red arrows) and more widespread LOF porosity (blue arrows). Upon closer examination (**Fig. 4B2**), LOF pores were intermixed between B_4C particles and *in situ* phases at random throughout the microstructure. For the Ti6Al4V-1.25B_4C-1.25BN composition produced at energy densities ranging from 21.5-25.3Jmm^{-3}, LOF porosity tended to be the dominant defect observed in the microstructure, with defects ranging from as small as submicron in size to 100-200μm in size, significantly larger in size and magnitude compared to any defects present in the Ti6Al4V-2.5B_4C-2.5BN composition (see **Fig. 5**). Despite LOF porosity, these microstructures were more crack-free than the Ti6Al4V-2.5B_4C-2.5BN compositions processed at various parameters. **Fig. 6** outlines some of the characteristic crack-formation observed in the microstructures. For the Ti6Al4V-2.5B_4C-2.5BN composition, the main cracking sources were more likely to be near partially-reacted B_4C and/or BN particles in the microstructure for the higher heat input of 41.9Jmm^{-3} (**Figs. 6A1 & 6A2**)., as opposed to more likely to form near LOF porosity in the case of 31.5Jmm^{-3} input energy (**Figs. 6B1 & 6B2**). Near the LOF pores of **Fig. 6B1**, a partially-fused Ti6Al4V particle is observed, further underscoring the source of these defects. For the Ti6Al4V-1.25B_4C-1.25BN composition, LOF porosity was also a main contributing factor to the defect and crack formation. These pores > 100µm tended to form initiation sites for cracks extended throughout the microstructure (see **Figs. 6C1 & 6C2**).

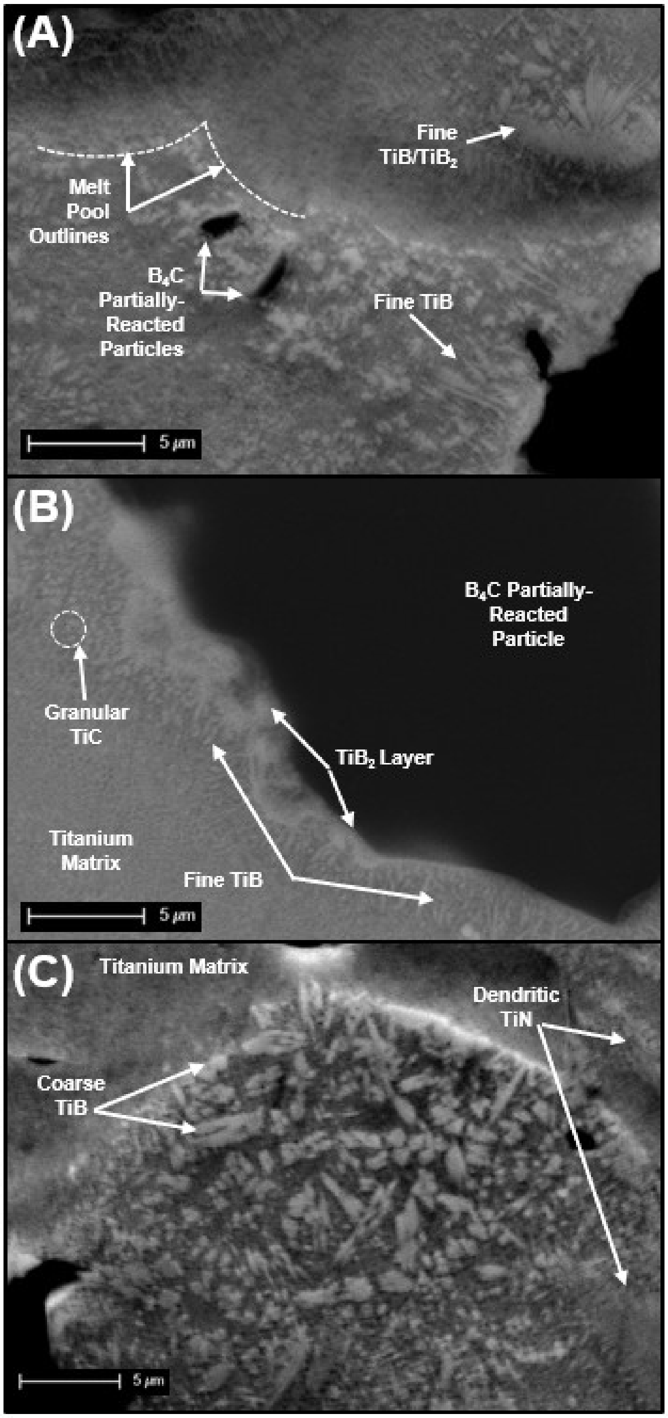

Figure 7: Characteristic high-magnification microstructures near melt pool outlines of Ti6Al4V-2.5B4C-2.5BN composition processed at 31.5 Jmm-3. Build direction is vertical.

Characteristic high-magnification microstructures of the *in situ* reactivity of the Ti6Al4V-2.5B_4C-2.5BN sample produced at 32Jmm^{-3} are shown in **Fig. 7**, and are characteristic of both the various processing parameters as well as the different ceramic-reinforced compositions in the study. Near melt-pool outlines (**Fig. 7A**), partially-reacted B_4C particles are observed as well as *in situ* TiB/TiB_2 networks forming from the decomposition of the B_4C reinforcing phase under laser heating. Looking closer at a partially-reacted B_4C particle (**Fig. 7B**), the formation of boride networks from the surface is readily evident. The reaction layer formed around the particle and reduced its overall size is embedded in it the titanium alloy matrix. BN particles reacting with the titanium alloy matrix to form TiN dendritic structures and TiB networks (**Fig. 7**) are also present in the microstructure, although less predominant reported in previous works with similar Ti-BN based systems. XRD analysis (**Fig. 8**) of the separate compositions reveals characteristic peaks for α-Ti (ICDD: 00-044-1294) in both the Ti6Al4V and Ti6Al4V-2.5B_4C-2.5BN composition within the 2theta range of 30-55°, and small peaks for TiB_2 (ICDD: 00-035-0741) at both 34.0° and 44.3° in the Ti6Al4V-2.5B_4C-2.5BN composition. It is noted here that there are peak overlaps of the characteristic β-Ti (ICDD: 98-015-1409) peak at 38.3°, and B_4C: (ICDD: 00-019-0178) at 38.3°, with B_4C referenced here because of its predominance in the microstructure as shown in **Figs. 4 & 5**.

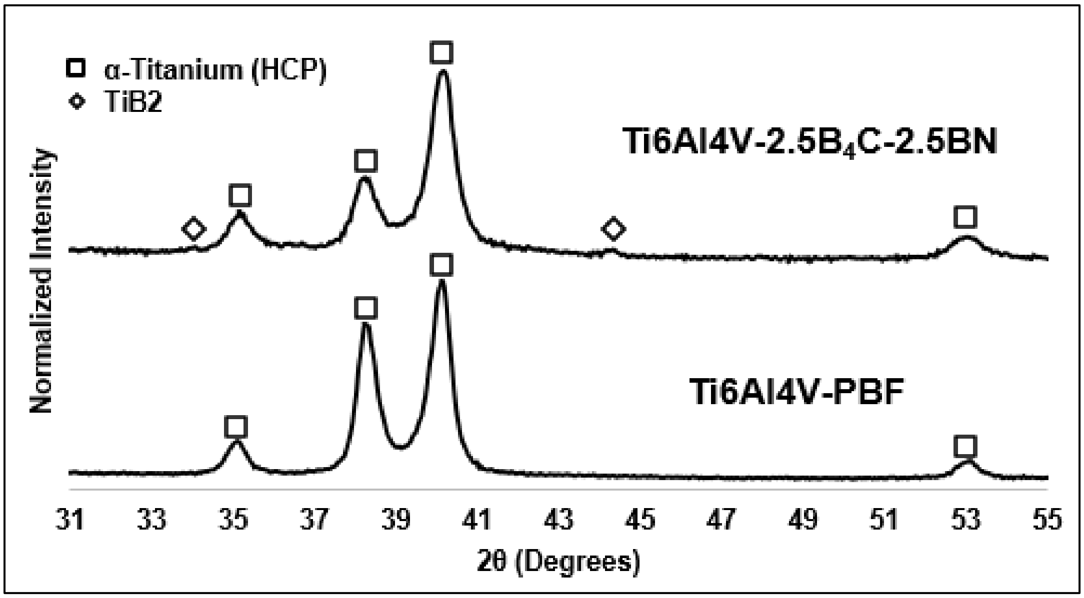

Figure 8: XRD analysis of variable input energy parameters of the Ti6Al4V-2.5B_4C-2.5BN composition.

The hardness and relative densities of each of the compositions are shown in **Figs. 9A & 9B, and Fig. 10.** The Ti6Al4V sample processed at the manufacturer-recommend parameters (63.0Jmm^{-3}) had an average hardness of 389 ± 7 HV$_{0.2/15}$, and was consistent across the entire build height (not shown), with a relative bulk density of 99.8 ± 0.03%. For the composite compositions, indent averages and standard deviations are shown for three main locations for each composition and parameter set: one near the ~0.5mm above the substrate in the bulk material, halfway up the build ~5mm, and one location near the top ~0.5mm away from the top surface) for the 10mm tall samples. It is important to note that there are differences when comparing a parameter set to a parameter set, but within a specific parameter set, the minimal difference was observed when considering the indentation location and the build height. The Ti6Al4V-2.5B$_4$C-2.5BN composition processed at 31.5Jmm^{-3} had an overall average hardness of 587 ± 25 HV$_{0.2/15}$, significantly higher than the Ti6Al4V processed without reinforcement (see **Fig. 9A**). This same composition exhibited a significant increase in hardness when processed at 34.5Jmm^{-3} and 41.9Jmm^{-3}, which had an overall average hardness of 774 ± 29 HV$_{0.2/15}$ and 811 ± 34 HV$_{0.2/15}$, respectively. A similar increasing trend was

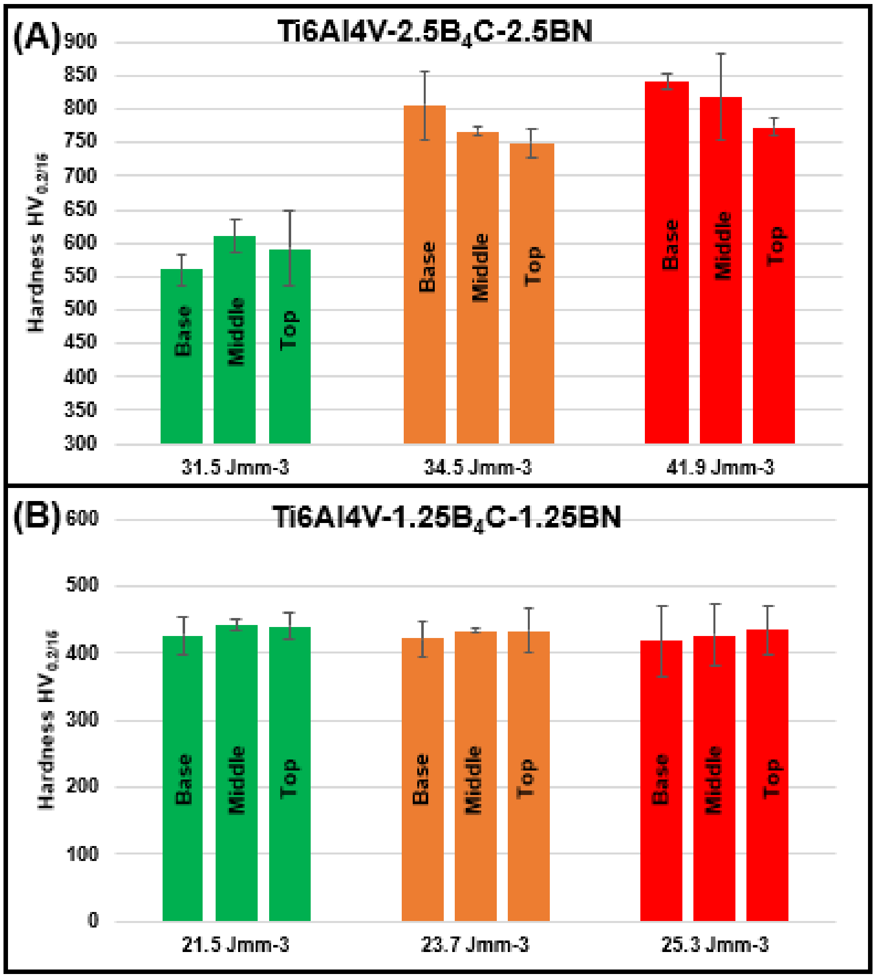

Figure 9: Hardness for each composition at different processing parameters. **(A)** Ti6Al4V-2.5B$_4$C-2.5BN. (B) Ti6Al4V-1.25B$_4$C-1.25BN. Note that Ti6Al4V processed at 63.0Jmm^{-3} had an average hardness of 389 ± 7 HV$_{0.2/15}$.

observed for the densities where samples produced at 31.5Jmm^{-3} had an average relative density of 95.9 ± 0.01% (measured relative to theoretical density value of 4.325 gcc^{-1}), and increased to 98.0 ± 0.02% and as high as 98.3 ± 0.01% for processing input energies of 34.5Jmm^{-3} and 41.9Jmm^{-3}, respectively. The Ti6Al4V-1.25B$_4$C-1.25BN composition processed at 21.5Jmm^{-3} had an average hardness of 436 ± 8 HV$_{0.2/15}$, slightly higher than the Ti6Al4V processed without reinforcement (see **Fig. 9B**). This same composition exhibited a significant increase in hardness when processed at 23.7Jmm^{-3} and 25.3Jmm^{-3}, which had an overall average hardness of 430 ± 7 HV$_{0.2/15}$ and 427 ± 8 HV$_{0.2/15}$, respectively, indicating a limited effect of processing parameters on the hardness for this composition. Similarly, for the relative density values, no significant trend was observed where samples produced at 21.5Jmm^{-3} had an average relative density of 94.7 ± 0.02% (measured relative to theoretical density value of 4.266 gcc^{-1}), and the others at 94.3 ± 0.01% and 93.9 ± < 0.01% for processing input energies of 23.7Jmm^{-3} and 25.3Jmm^{-3}, respectively.

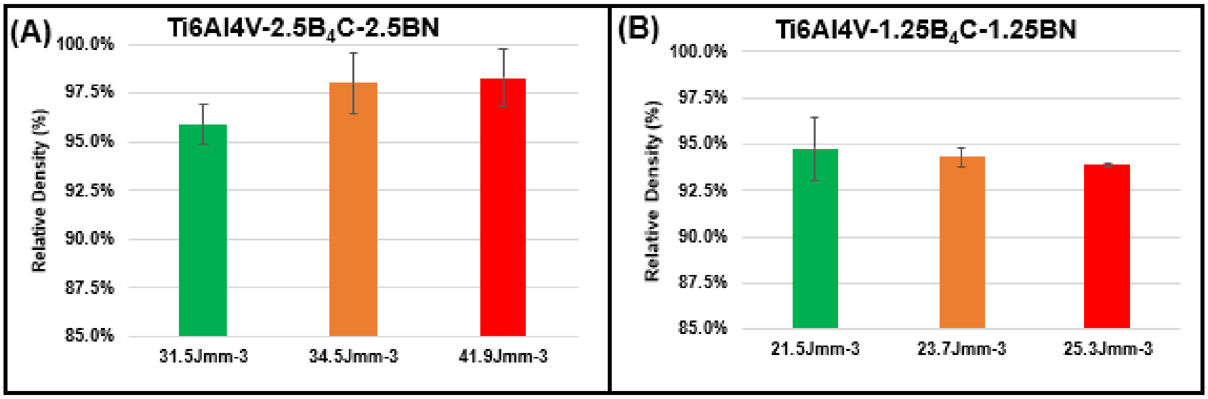

Figure 10: Relative density measurements for each composition. **(A)** Ti6Al4V-2.5B$_4$C-2.5BN. **(B)** Ti6Al4V-1.25B$_4$C-1.25BN. Note that Ti6Al4V processed at 63.0Jmm^{-3} had an average relative density of 99.8 ± 0.03%.

A comparison of the partially-reacted B_4C particles in the microstructures of both compositions and two different energy inputs (~20-30% difference) is shown in **Fig. 11**. The B_4C as-sieved < 63µm particle distribution is most clearly has the highest end of both average size and distribution with average size and area of 45.3µm and 1.47e-3µm^2, respectively. For the Ti6Al4V-2.5B_4C-2.5BN composition, these values are significantly decreased to 29µm and 0.60e-3µm^2 and 23.5µm and 0.49e-3µm^2 for the processing energy inputs of 31.5Jmm^{-3} and 41.9Jmm^{-3}, respectively. For particle size, the distribution mainly was Gaussian in the as-sieved state but tended to be low-end distributed in the as-processed condition(s) and shifted towards the smaller particle sizes, and the higher energy input samples processed at 41.9Jmm^{-3} tended to have the lowest end distribution compared to the 31.5Jmm^{-3} processing parameters. Comparatively, the particle area had a much more variable distribution (non-Gaussian), with overall areas shifted furthest for the highest-end energy density processing parameters at 41.9Jmm^{-3} . Comparatively, for the Ti6Al4V-1.25B_4C-1.25BN_composition, the particle size and area values are similarly decreased relative to the as-sieved condition to 29µm and 0.63e-3µm^2

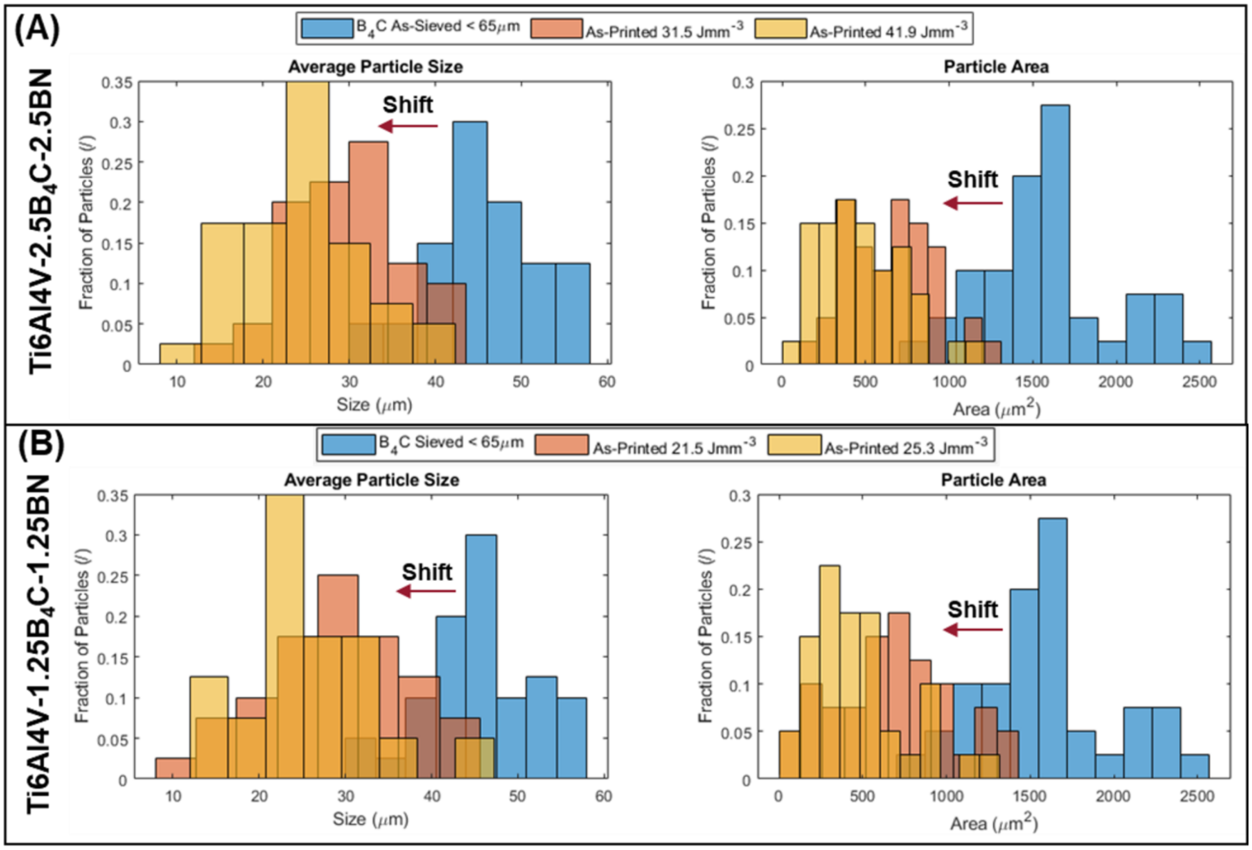

Figure 11: Comparison of composition and processing parameter set on the size and area of partially-reacted B_4C particles in the remaining microstructure. **(A)** Ti6Al4V-2.5B_4C-2.5BN. **(B)** Ti6Al4V-1.25B_4C-1.25BN.

and 25.0μm and 0.39e-3μm^2 for the processing energy inputs of 21.5Jmm^{-3} and 25.3Jmm^{-3}, respectively. For particle size, the distribution mainly was Gaussian in the as-sieved state but tended to be low-end distributed in the as-processed condition(s) and shifted towards the lower particle sizes, and the higher energy input samples processed at 25.3Jmm^{-3} tended to have the lowest end distribution compared to the 21.5Jmm^{-3} processing parameters. The particle area had a much more variable distribution (non-Gaussian), with overall areas shifted furthest for the highest-end energy density processing parameters at 25.3 Jmm^{-3} than the as-sieved condition 21.5Jmm^{-3}.

3.3 Isothermal oxidation at 850°C: Isothermal mass gain plots and bulk sample hardness values and oxide scale thickness are shown in **Fig. 12**. For all compositions, consistency was exhibited when comparing the 25h and 50h runs, with both sets of samples exhibiting similar kinetic regimes and overall mass gain. For the Ti6Al4V composition, parabolic kinetics were exhibited throughout the entire testing, with final normalized mass gain values of 9.1 mgcm^{-2} and 14.5 mgcm^{-2} for 25h and 50h testing, respectively. For the Ti6Al4V-1.25B_4C-1.25BN composition, the final normalized mass gain values were 8.5 mgcm^{-2} and 12.5 mgcm^{-2}, showing a 7% and 16% decrease in mass gain after 25h and 50h of testing in comparison to Ti6Al4V. The final normalized mass gain values for the Ti6Al4V-2.5B_4C-2.5BN composition were 7.2 mgcm^{-2} and 9.6 mgcm^{-2} for 25h and 50h of testing, which resulted in as much as 21% and 39% decrease in mass gain after 25h and 50h of testing. From the bulk hardness values in **Fig. 12B**, Ti6Al4V exhibited a decreasing trend from 389 ± 7 $HV_{0.2/15}$ to 339 ± 9 $HV_{0.2/15}$ between the as-processed conditions as-oxidized at 50 hours. In comparison, both ceramic containing compositions exhibited an initial increase in the hardness after 25h of testing and then non-significant increases afterward at the 50h test mark, with much wider standard deviations than the Ti6Al4V composition alone. For the Ti6Al4V-1.25B_4C-1.25BN composition, the hardness in the as-processed condition was 436 ± 8 $HV_{0.2/15}$ but subsequently increased to 545 ± 64 $HV_{0.2/15}$ and 555 ± 37 $HV_{0.2/15}$ after 25h and 50h of testing, indicating a 25-27% increase in bulk hardness due to the high-temperature environment exposure. For the Ti6Al4V-2.5B_4C-2.5BN composition, the hardness in the as-processed condition was 587 ± 25 $HV_{0.2/15}$ but subsequently increased to 670 ± 59 $HV_{0.2/15}$ and 690 ± 87 $HV_{0.2/15}$ after 25h and 50h of testing, indicating a 14-18% increase in bulk hardness due to the high-temperature environment exposure. The graph in **Fig. 12C** and the EDS images in **Fig. 13** highlight the effects of ceramic reinforcement on the scale progression. For Ti6Al4V, the scale grew to a value of 59.0 ± 1.1μm after 25h and then to

102.1 ± 6.2μm after 50h of testing. For the Ti6Al4V-1.25B_4C-1.25BN composition, the scale grew to a value of 51.5 ± 6.7μm after 25h and then remained nearly constant at 49.9 ± 3.4μm after 50h of testing. Similarly, the Ti6Al4V-2.5B_4C-2.5BN scale grew to a value of 24.9 ± 4.2μm after 25h and then remained nearly constant, growing to a final value of 27.3 ± 2.3μm after 50h of testing, nearly a 4X decrease in the oxide thickness relative to Ti6Al4V after 50h of testing. The corresponding EDS images (**Fig. 12**) demonstrate the significant oxide scale thickness difference apparent in the cross-section of Ti6Al4V and the ceramic-containing compositions. Additionally, the thickness of the 2.5wt% reinforcement composition was significantly thicker than the 5wt% composition. All oxides spalled, which has been previously reported upon cooling from temperatures over 850°C during testing [12]. Additionally, the Ti6Al4V oxide retained varying Al-rich and Ti-rich composition regions, indicating a layered oxide compared to the ceramic compositions, which exhibit mainly Ti-rich regions, with some Al-rich areas spread throughout the oxide layer.

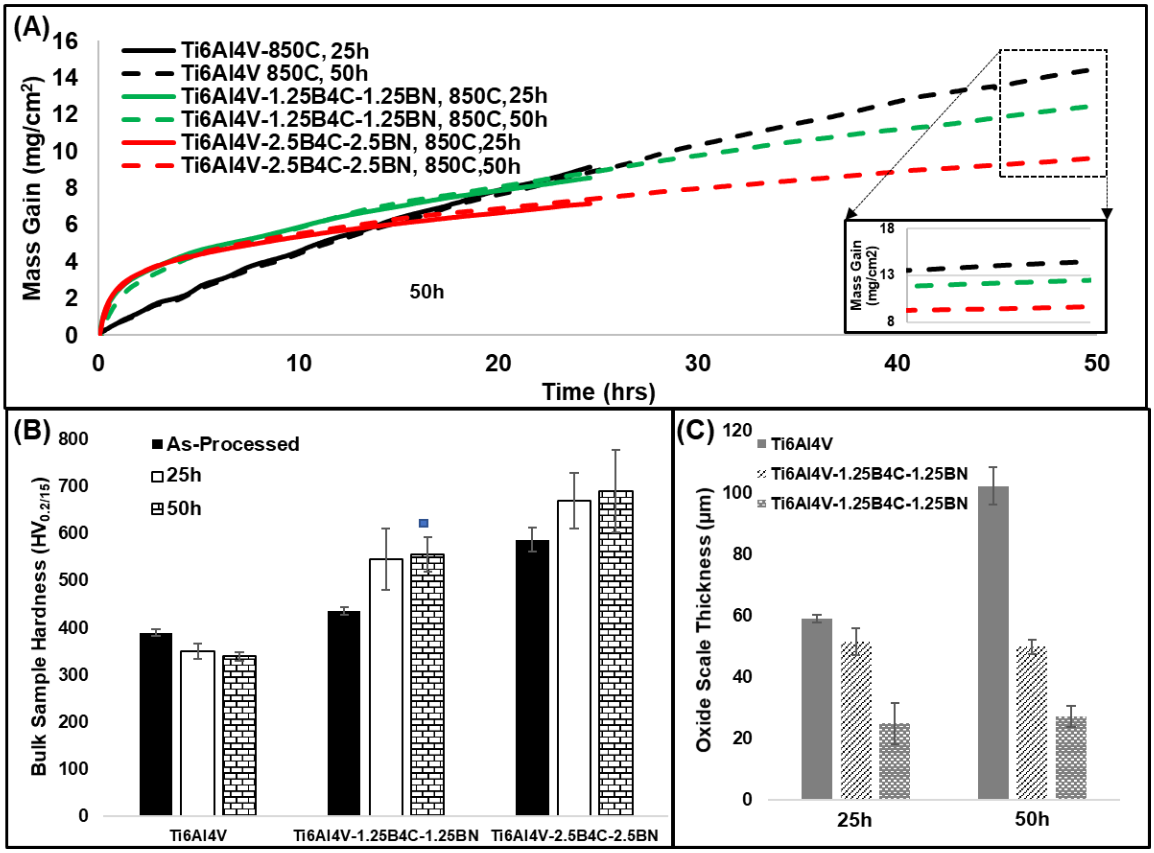

Figure 12: Oxidation testing results for as-printed Ti6Al4V-1.25B_4C-1.25BN and Ti6Al4V-2.5B_4C-2.5BN in comparison to Ti6Al4V. **(A)** Thermogravimetric mass-gain curves. **(B)** Sample hardness post-testing with as-processed hardness shown for comparison. **(C)** Oxide scale thickness (compare with **Fig. 13**.)

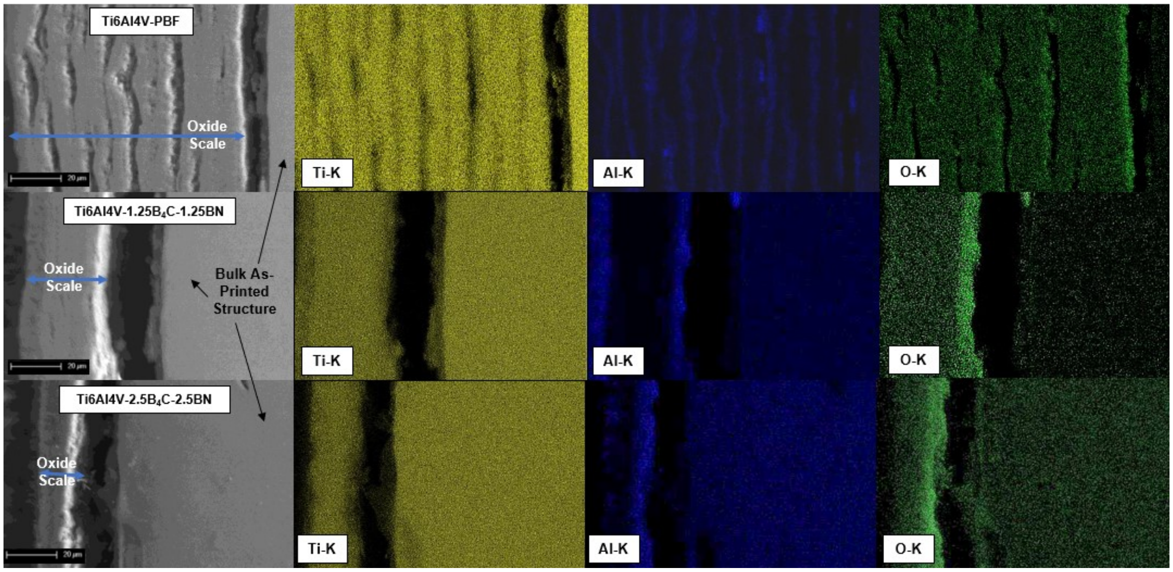

Figure 13: EDS analysis of oxide scales for Ti6Al4V-1.25B_4C-1.25BN and Ti6Al4V-2.5B_4C-2.5BN in comparison to Ti6Al4V for 50h isothermal oxidation test.

3.3 Demonstration parameter set samples and lattice structures: Vertically-varying parameter set samples were manufactured with different scanning speeds (and effective energy input) as shown in **Fig. 14**, using the Ti6Al4V-2.5B_4C-2.5BN composition at 31.5Jmm^{-3} and a 20% decrease in scanning speed resulting in an effective energy input of 37.8Jmm^{-3}. A sample with "sandwiched" parameters, i.e., high energy input (39Jmm^{-3}) for two sections at 0.5mm height, was fabricated (and the other processing parameter sections at double that height), as well as a sample with two sections of moderate input energy height of 0.5mm (32Jmm^{-3}). Cracks formed within both samples nearest to the regions with higher input energy, indicating significant stress and crack formation at the interfaces between the different parameter sets. The sample from **Fig. 14A** was able to successfully process for the entire 5mm tall sample, whereas the sample from **Fig. 14B** (which had much larger regions of high input energy density) could not complete printing and had to be stopped in the final printing parameter region. Additional lattice structures were printed with the Ti6Al4V-2.5B_4C-2.5BN composition at 31.5Jmm^{-3} with 450μm designed strut diameters and variable lattice diamond-based unit cells to varying the effective porosity of the structure. As shown in **Fig. 15**, successful processing was exhibited for the lattice structures at each of the designed porosities (50%, 65%, and 85%), with ~5-10% difference in the overall strut thicknesses on each of the different structures, indicating geometric stability and the ability to produce complex, high-resolution components using this advanced composite composition. Additionally, the lattice's surface showed a comparable reflectivity to the Ti6Al4V samples processed at Ti6Al4V's optimized parameters, indicating surface qualities comparable to Ti6Al4V even with the added ceramic reinforcement and reduced energy input.

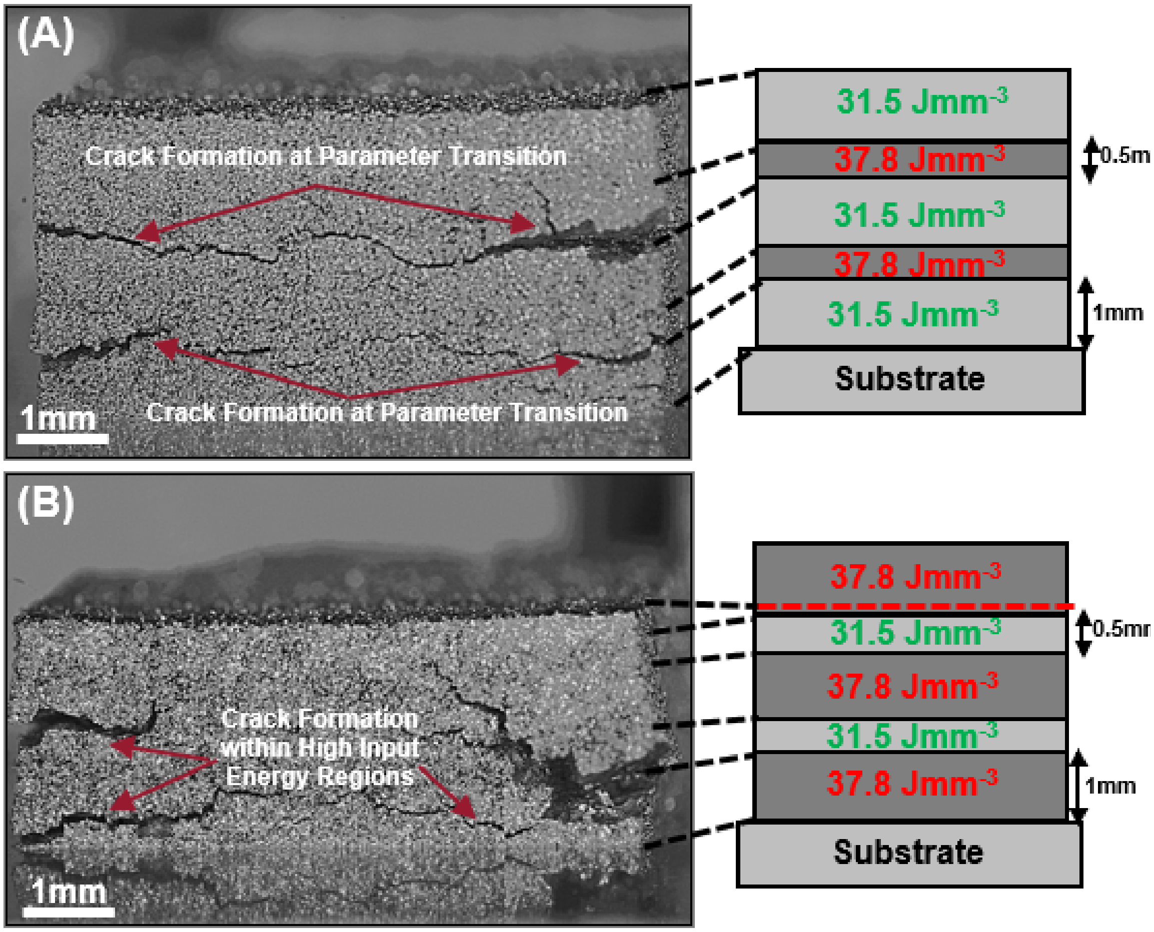

Figure 14: Effects of variable input energy density at different heights within the build, demonstrating the propensity for crack formation at high input energy density input.

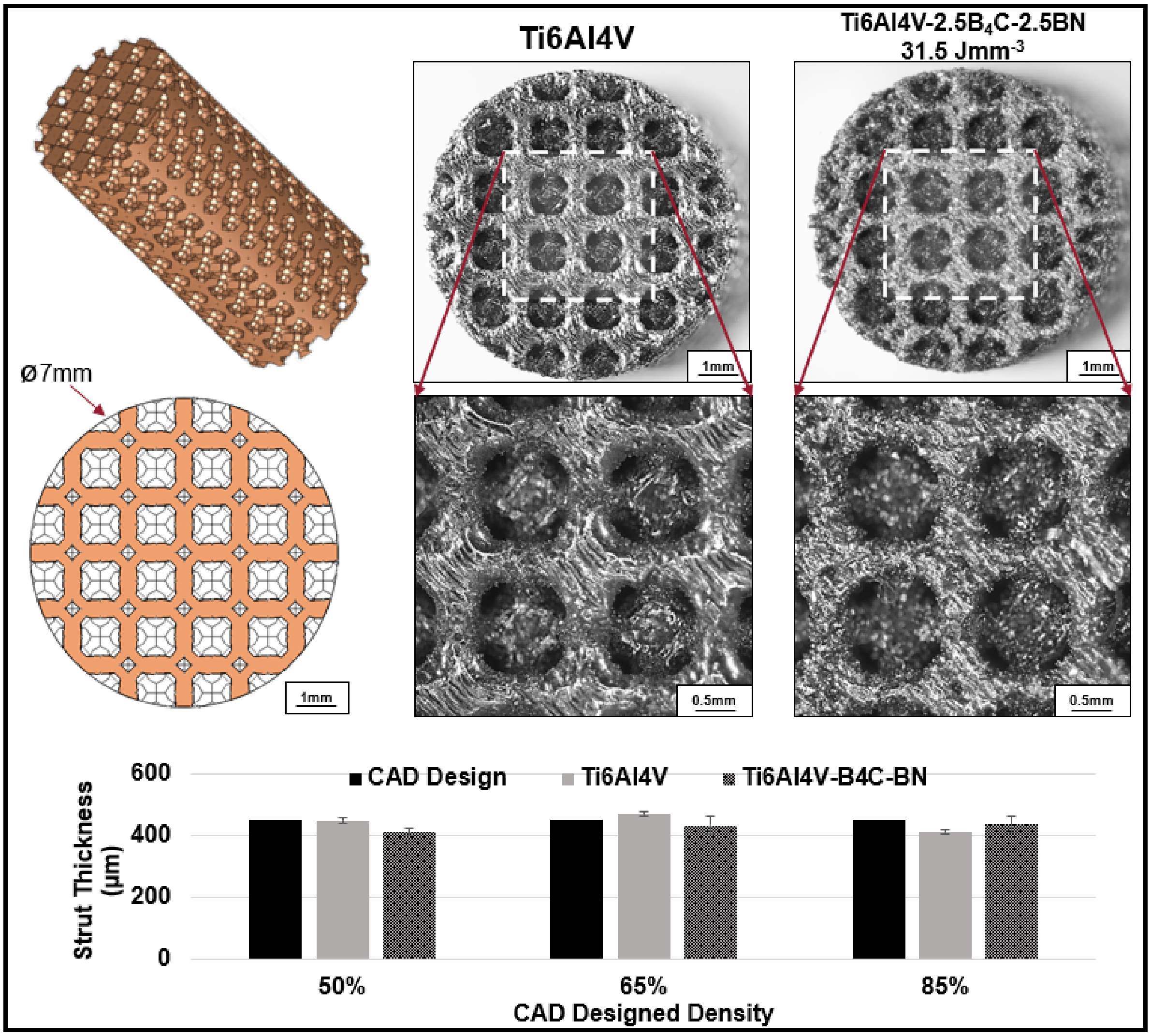

Figure 15: Processing accuracy of diamond-unit cell lattice structures comparing the accuracy of strut-design thickness to the CAD dimensions for a Ti6Al4V-2.5B_4C-2.5BN composition processed at 31.5Jmm^{-3}.

4. Discussion

Previous work has shown that processing composite feedstocks via SLM can produce materials and structures significantly improved properties over the base matrix material [3,7–10]. The composition range of titanium-boron carbide-boron nitride studied herein was previously developed via DED and is evaluated here for processability via SLM for use in applications requiring wear and/or high-temperature oxidation resistance. Hardness, X-ray diffraction, high-magnification SEM imaging, and analysis aids in understanding some of the effects of input processing parameters on the resulting processability of this composite material system via powder-bed-based AM methods.

4.1 *In situ m*icrostructure formation within the Ti6Al4V-B_4C-BN composites: In comparison to previous work within the titanium-boron carbide-boron nitride system via DED [10], the microstructures in the present study were less TiN/TiB/TiC dominant as opposed to TiB/TiB_2 dominant and maintaining a homogenous distribution of B_4C particles, TiB/TiB_2 networks, and partially-reacted BN particles. The formation of the boride networks follows from reactions of both boron carbide and boron nitride with the abundant titanium matrix under laser heating as previously described as such [8,10,17]:

$$5\mathrm{Ti} + \mathrm{B_4C} \rightarrow 4\mathrm{TiB} + \mathrm{TiC} \quad (2)$$

$$3\mathrm{Ti} + 2\mathrm{BN} \rightarrow \mathrm{TiB_2} + 2\mathrm{TiN} \quad (3)$$

Within the abundance of a titanium matrix, a thin TiB_2 reaction layer surrounds B_4C particles as previously shown [8,18], and under further reaction, the layer forms a refined TiB needle-like phase surrounding the B_4C particle. In the present study, this TiB_2 phase was directly confirmed from XRD analysis (**Fig. 8**), and from **Fig. 7A**, partially-reacted B_4C particles are observed near melt pool outlines with what appears to be a trace of a nearly-fully reacted B_4C particle within the solidified melt pool. This indicates the differing degree of reactivity within the bulk structure depending on the location of the different-sized particles in the solidification structure. Additionally, in **Fig. 7B**, the characteristic TiB_2 reaction layer was observed, which was typical when imaging at high magnifications within all compositions and processing parameter ranges. The granular TiC phase (as previously reported) was present between TiB needle within the overall titanium matrix [8]. Further, the resulting particle size of the B_4C particles was significantly shifted to a lower range than the starting < 63μm sieve size, indicating significant reaction during processing and the formation of in situ reinforcing phases present in the microstructure (see **Fig. 11**). Comparatively, BN particles were not as readily present in the microstructure as compared to previous studies [10,12], but a partially-reacted particle is shown in **Fig. 7**C, where some dendritic structures (corresponding to TiN phase) are present [10], as well as a predominant boride-like microstructure with additional BN decomposition in the titanium matrix. These microstructures correspond to the decomposition of BN detailed in ref. [19], which describes the inward diffusion of N_2, formation of TiN in dendrites, and needle-like formation of TiB/TiB_2 during laser processing.

In general, these microstructural phases and morphologies have demonstrated increased oxidation resistance [10], mechanical properties [20], and wear resistance [21,22] in comparison to titanium and its alloys alone, indicating the effectiveness of these microstructures if this material system can be processed crack-free via SLM. The hardness and relative densities recorded in the present study for the Ti6Al4V-2.5B_4C-2.5BN (587-811 $HV_{0.2/15}$, 95.9-98.3%) were comparable in some cases improved, over other titanium-matrix composites of similar overall reinforcement processed using SLM [23]. For a Ti-7.55wt%TiC composite, Gu et al. (2012) reported 98.3% density and highly reactive TiC microstructures resulting in the hardness of 577 $HV_{0.2}$ [24]. Additionally, Xia et al. (2017) reported a similar hardness of 577 $HV_{0.2}$ for a composite of Ti-5wt%TiC, indicating a comparable hardness and build quality to the Ti6Al4V-2.5B_4C-2.5BN composition processed at 31.5Jmm^{-3} of 587 $HV_{0.2/15}$ and 95.9% relative density in the present study, which exhibited minimal bulk cracking during processing.

4.2 Effects of input energy density on processing outcomes: As shown in **Figs. 2 & 3**, the processing range for the reinforced composites structures was nearly 30-50% lower than Ti6Al4V's (of 63.0Jmm^{-3}) at ~20-32Jmm^{-3}, indicating the immense impact that ceramic reinforcement has on the processability range. SLM is a complex, high cooling rate process with several key input parameters determining a particular material's ability to be processed via this method. In this particular study, input energy density (as calculated via Simchi's equation) can be used to delineate the challenges of working with such a reactive material system [14]. Generally, higher laser power is directly correlated with higher energy input into the material, whereas scanning speed, hatch spacing, and layer thickness are inversely related to the amount of energy input into the material (see **Eq. 1**). Additionally, because many of the printed composite samples protruded from powder bed upon layering, the hard-recoater and compaction can contribute an additional mechanical force into the sample during printing. This adds to an already complex combination of thermal and mechanical loads due to processing-induced stress and additional heat input due to the exothermic reactions during high-temperature processing. Further, the potential added load from the recoater is much larger at high input energy because higher distortion is observed out of the build plane, increasing the contact area and contributing to higher induced stresses in bulk printed material and subsequent propensity for large-scale cracking and processing failure. In these samples, this was noted by loud clanging of the recoater hitting the top of the samples, at times ending the build due to torque overload on the recoater.

Because of this, it is envisioned that a soft recoater may increase processability at high input energy density by lowering the induced mechanical load, potentially leading to successful samples with higher hardness and relative density.

For the Ti6Al4V-2.5B_4C-2.5BN composition, cracking and process failure were directly related to the higher input energy densities applied during laser processing. Tracking of the B_4C size distribution from the as-sieved condition to the as-printed microstructure alone indicates how reactive these composites are during processing, with ~36-48% decreases in average particle size and ~57-73% decreases in particle area on top of drastically shifted distributions when looking at both composite compositions (see **Fig. 11**). Similar overall distribution ranges (and average size/area) were observed for both the composites produced with a composition of Ti6Al4V-2.5B_4C-2.5BN and Ti6Al4V-1.25B_4C-1.25BN, but there is a slight shift downward in both the size and area distribution for both compositions when considering an increase in energy input from 31.5 to 41.9 Jmm^{-3} in the Ti6Al4V-2.5B_4C-2.5BN composition and 21.5 to 25.3 Jmm^{-3} for Ti6Al4V-1.25B_4C-1.25BN, indicating increased reactivity and propensity to form *in situ* phases (and brittle microstructures/cracks) that further can cause processing failure at higher input energy density. This decrease in the overall B_4C size distribution is directly linked to the increase *in situ* phase formation in the bulk matrix and increase in hardness for higher input energy samples for the Ti6Al4V-2.5B_4C-2.5BN composition, which had an ~15% average hardness increase from 587 ± 25 $HV_{0.2/15}$ to 811 ± 34 $HV_{0.2/15}$ when processing at 31.5 Jmm^{-3} and 41.9 Jmm^{-3}, respectively. This increase was not observed for the Ti6Al4V-1.25B_4C-1.25BN composition, likely due to the reduced amount of overall reinforcement and the fact that hardness indents were taken in the matrix where only *in situ* reinforcement was able to contribute to hardness increase, meaning that the lower overall ceramic reinforcement and corresponding *in situ* phase formation were not able to affect the overall matrix hardness in comparison to the larger ceramic reinforcement amount.

Increases in hardness (and corresponding *in situ* reactivity) contributed to bulk microstructural cracking through reinforcing phases for Ti6Al4V-2.5B_4C-2.5BN samples produced above 31.5 Jmm^{-3} (see **Fig. 4A & 4B**). These cracks were networked between different B_4C and BN particles (see **Fig. 6A1 & 6A2**), indicating an overall brittle matrix due to *in situ* reactivity that could not arrest cracks under repeated cyclic loading during processing. Because of this, samples produced above 31.5 Jmm^{-3} tended to fail or have extreme material pullout/cracking and debonding from the substrate, as shown in **Fig. 2** for the sample produced at

41.9 Jmm^{-3}. Comparatively, samples produced at 31.5 Jmm^{-3} had mostly crack-free microstructures and were able to be processed without any external cracking or debonding, but they did exhibit some small-scale cracking in the microstructure, as shown in **Fig. 6B1 & 6B2**. The cracks were highly localized and did not cause bulk failure (see **Fig. 4B1 &** 4**B2**) as most cracks could be arrested in the matrix material. These cracks were consistently found only near LOF pores present in the microstructure, indicating a tendency for the stress concentrations near the pores to cause cracking to alleviate stress during the cyclic thermal and mechanical loads during processing (that are subsequently arrested in the titanium matrix). The increased porosity in the Ti6Al4V-2.5B_4C-2.5BN composition processed at 31.5 Jmm^{-3} in comparison to 41.9 Jmm^{-3} (namely 95.9% vs. 98.2%) meant that there was an increased amount of pores in the microstructure to cause internal stress concentration relative to the composition processed at 41.9 Jmm^{-3}, which predominantly saw processing failure due to *in situ* reactivity. From these observations, there is a precise balance between decreasing the input energy to avoid cracking due to *in situ* reactivity and providing enough input energy to keep the bulk density as high as possible to limit porosity, contributing to processing inconsistencies at low input energy. This line of reasoning also applies to the Ti6Al4V-1.25B4C-1.25BN composition that did not exhibit any significant increase in processability or different processing range compared to the Ti6Al4V-2.5B_4C-2.5BN composition at similar overall input energy ranges. **Figs. 5 & 6C1 & 6C2** show a significantly larger amount of LOF pores in the microstructure that contributes to cracking in the Ti6Al4V-2.5B_4C-2.5BN composition processed at lower input parameter ranges. Despite a 50% reduction in ceramic reinforcement, processing failure is also attributed to in situ reactivity at high input energy ranges near Ti6Al4V and the high LOF porosity that leads to cracking in the microstructure input energy ranges. Overall, the Ti6Al4V-2.5B_4C-2.5BN composition processed in the low-end of the input energy range produced the most desirable characteristics such as high relative density, hardness, and process reliability compared to higher input energy at the same composition as well as any processed composition with the reduced ceramic reinforcement. Interestingly, the reduced input energy density requirement has the unintended consequence of reducing the required power input for fabricating samples with these compositions, which would be desirable for industrial users concerned with overall power consumption during manufacturing at scale.

Because the samples produced at higher input energy for the Ti6Al4V-2.5B_4C-2.5BN had higher bulk density and hardness, it was envisioned that adjusting processing parameters during the print might stimulate reduced residual stress and processing failure while also achieving more improved hardness and bulk density in a processed component. Samples A and B from **Fig. 14** highlight that having even a small section of input parameters higher than ~31.5Jmm^{-3} will result in processing inconsistency and failure at the interface of the two processing sets, even if the heights of the high input energy are relatively thin or thick in comparison to the optimal processing parameters. With the modification of the recoater blade to a soft style to decrease the additional induced stress, it is envisioned that some high input energy density regions could be introduced to create functionally-graded composites with regions of high hardness and then corresponding lower input energy density regions of lower overall hardness but higher ductility.

4.3 Effects of composition on oxidation performance: Ceramic reinforcement significantly prevented continued oxidation at high temperatures within the as-printed titanium composites. After 50hs of testing, as high as a 39% decrease in the overall mass gain was achieved with 5wt% ceramic (i.e., the Ti6Al4V-2.5B4C-2.5BN composition), indicating a significant difference decrease in the oxidized mass on the surface of the samples in comparison to Ti6Al4V alone. This was further evidenced from the high-magnification cross-section micrographs that show a significantly decreased oxide layer (nearly 4X decrease compared to Ti6Al4V), highlighting the efficacy of the ceramic reinforcement to alleviate high-temperature oxidation in the composites. Interestingly, the Ti6Al4V composite exhibited a nearly-parabolic kinetic regime throughout the test, while the ceramic compositions both exhibited a transition from linear to parabolic. This difference is attributed to the increased porosity in the ceramic composition compared to the purely Ti6Al4V composition, which leads to increased surface area for oxidation and mass gain in the early time period of the test when the initial scale is spreading over the surface of the samples. Cracks and pores were also evident in the work of Ma et al. (2019), which still reported enhanced oxidation resistance of the TiAl-TiC composites at high temperatures [25]. Despite this initial linear regime, both composite compositions in the present study exhibited parabolic kinetics with significantly slower oxidation kinetics in comparison to Ti6Al4V further into testing, indicating a slowed diffusion of titanium to the oxide surface due to the presence of partially-reacted and *in situ* reinforcing phases in the microstructure that significantly decrease the available titanium and provide a diffusion barrier for the titanium migration to the surface, thus decreasing the overall oxidation mass gain over time. Because the Ti6Al4V-1.25B_4C-1.25BN composition maintained a reduced (50% relative to Ti6Al4V-2.5B_4C-

2.5BN) reinforcement amount, the overall effect on the oxidation was reduced, and only a 16% decrease in the overall mass gain was observed after 50hs of testing, albeit still providing a significant barrier to titanium diffusion and further oxidation. It was found in our previous work that utilized both Arrhenius analysis and XRD on CPTi-B4C-BN (pure titanium matrix) that rutile (TiO_2) was the main reaction product on the surface of the as-oxidized samples [10]. In the current work, this was further substantiated from the EDS images showing the presence of titanium in the oxide layer, as well as some aluminum-based phase, most likely Al_2O_3, which was reported from work in Ma et al. (2019), who was studying the growth of oxide on the surface of titanium-based metal matrix composites with similar oxidizing elements present in the microstructure [25]. Because of the aluminum presence in the matrix within the current work, a multi-layer oxide composed of TiO_2 and Al_2O_3 can be anticipated at high temperatures. Despite the decreased overall oxidation of the ceramic compositions compared to the titanium-based matrix, continued reactivity and increased hardness were observed after 25h of testing. Both ceramic containing compositions exhibited an initial increase in the hardness after 25h of testing and then non-significant increases afterward at the 50h test mark, indicating an initial increase in the reactivity; however, less reaction between the 25h and 50h marks. This phenomenon has been observed previously in these composites and must be considered in the direct application of these materials at high temperatures when considering properties after prolonged exposure to oxygen environments [10,12]. Because of the desirable oxidation characteristics, it is envisioned that future studies will characterize the mechanical properties at temperature to understand further the potential applications and utilization of these composites produced using SLM.

4.5 Part fabrication: Because the Ti6Al4V-2.5B_4C-2.5BN could be processed at reduced input energy, it was envisioned that complex geometries could be fabricated, such as lattice structures (**Fig. 15**). These structures were produced within 5-10% of CAD dimensions (measured in the smallest portion of the strut, i.e., between joining strut sections, perpendicular to the build direction) at the optimized parameters of 31.5Jmm^{-3}, indicating this composite material system's ability to be used in applications requiring high oxidation resistance and strength compared to Ti6Al4V with the same benefits of reduced overall density and availability of materials in the process chain that these *in situ* composites offer through the reaction-based additive manufacturing process.

5. Conclusions

Titanium premixed with both 2.5wt% and 5wt% total reinforcement of boron nitride (BN) and boron carbide (B_4C) was processed via selective laser melting to understand processing parameters effects on the *in situ* reactive characteristics of the composites as well as cracking/build failure during processing. 10mm cubes were fabricated under a wide array of parameters to understand how energy density influences the resulting exothermic reactions between feedstocks and crack formation due to the transient thermal nature of the process. Microstructural analysis revealed that higher energy densities significantly deter the composites' processability regardless of overall wt% ceramic reinforcement, directly related to the continued *in situ* reactions that form during processing that lead to brittle microstructures. A 50% decrease in overall energy density compared to Ti6Al4V was required to avoid processing failure of this composition due to the high *in situ* reactivity, and the reduction of overall ceramic reinforcement amount did not improve the processability due to increased porosity in the microstructure. Composites were fabricated with as high as 98.3% relative density, and high-temperature oxidation testing revealed a 39% decrease in oxidation mass gain compared to Ti6Al4V due to the addition of ceramic reinforcement, indicating the efficacy of this approach towards tailoring titanium matrix composites for high-temperature applications. Lattice-based demonstration structures were fabricated at optimized parameters to demonstrate this technology's efficacy in fabricating complex components with advanced, reactive composite material systems. Our results indicate that selective laser melting can be utilized to create advanced composite materials and structures by carefully controlling input processing parameters related to the *in situ* reactivity of the feedstock materials. Further, material systems can be developed from powder-flow processes transitioned to powder-bed-based processing methods, providing a significant cost benefit to manufacturers focused on developing new materials via laser-based AM processes.

6. Acknowledgements

The authors would like to acknowledge financial support from the National Science Foundation under the grant number NSF-CMMI 1934230 (PI - Bandyopadhyay) and the Joint Center for Aerospace Technology Innovation (JCATI, Seattle, WA) grant in collaboration with the Boeing Company (Seattle, WA). The authors would also like to acknowledge financial support from JCDREAM (Seattle, WA) towards purchasing metal additive manufacturing facilities at WSU.

7. Declaration of Interest

The authors declare no conflict of interest.

8. References

[1] A. Bandyopadhyay, K. D. Traxel, S. Bose. Nature-inspired materials and structures using 3D-Printing. Mater. Sci. & Eng. R. (2021). doi: 10.1016/j.mser.2021.100609

[2] T. M. Pollock, A.J. Clarke, S.S. Babu, Design and Tailoring of Alloys for Additive Manufacturing, Metall. Mater. Trans. A Phys. Metall. Mater. Sci. (2020). doi:10.1007/s11661-020-06009-3.

[3] L.-C. Zhang, H. Attar, Selective Laser Melting of Titanium Alloys and Titanium Matrix Composites for Biomedical Applications: A Review, Adv. Eng. Mater. 18 (2016) 463–475. doi:10.1002/adem.201500419.

[4] S. Liu, Y.C. Shin, Additive manufacturing of Ti6Al4V alloy: A review, Mater. Des. 164 (2019) 107552. doi:10.1016/j.matdes.2018.107552.

[5] K. D. Traxel, A. Bandyopadhyay, Reactive-deposition-based additive manufacturing of Ti-Zr-BN composites, Addit. Manuf. 24 (2018). doi:10.1016/j.addma.2018.10.005.

[6] H. Attar, M. Bönisch, M. Calin, L.C. Zhang, S. Scudino, J. Eckert, Selective laser melting of in situ titanium-titanium boride composites: Processing, microstructure and mechanical properties, Acta Mater. 76 (2014) 13–22. doi:10.1016/j.actamat.2014.05.022.

[7] B. Vrancken, S. Dadbakhsh, R. Mertens, K. Vanmeensel, J. Vleugels, S. Yang, J.-P. Kruth, Selective Laser Melting process optimization of Ti–Mo–TiC metal matrix composites, CIRP Ann. 68 (2019) 221–224. doi:10.1016/j.cirp.2019.04.120.

[8] M. Xia, A. Liu, Z. Hou, N. Li, Z. Chen, H. Ding, Microstructure growth behavior and its evolution mechanism during laser additive manufacture of in-situ reinforced (TiB+TiC)/Ti composite, J. Alloys Compd. 728 (2017) 436–444. doi:10.1016/j.jallcom.2017.09.033.

[9] N. Kang, P. Coddet, Q. Liu, H. Liao, C. Coddet, In-situ TiB/near α Ti matrix composites manufactured by selective laser melting, Addit. Manuf. 11 (2016) 1–6. doi:10.1016/j.addma.2016.04.001.

[10] K. D. Traxel, A. Bandyopadhyay, Influence of in situ ceramic reinforcement towards tailoring titanium matrix composites using laser-based additive manufacturing, Addit. Manuf. 31 (2020) 101004. doi:10.1016/j.addma.2019.101004.

[11] H. Sahasrabudhe, A. Bandyopadhyay, Additive Manufacturing of Reactive In Situ Zr Based Ultra-High Temperature Ceramic Composites, Jom. 68 (2016) 822–830. doi:10.1007/s11837-015-1777-x.

[12] J. D. Avila, A. Bandyopadhyay, Influence of boron nitride on reinforcement to improve high temperature oxidation resistance of titanium, J. Mater. Res. (2019) 1–11. doi:10.1557/jmr.2019.11.

[13] A. Bandyopadhyay, K. D. Traxel, Invited review article: Metal-additive manufacturing—Modeling strategies for application-optimized designs, Addit. Manuf. 22 (2018) 758–774. doi:10.1016/j.addma.2018.06.024.

[14] A. Simchi, H. Pohl, Effects of laser sintering processing parameters on the microstructure and densification of iron powder, Mater. Sci. Eng. A. 359 (2003) 119–128. doi:10.1016/S0921-5093(03)00341-1.

[15] ASTM Standard E384-16, Test Method for Microindentation Hardness of Materials, ASTM International, West Conshohocken, PA, PA, 2016. doi:10.1520/E0384-16.

[16] ASTM Standard C1327, W. Conshohocken, ASTM Standard C1327, Test Method for Vickers Indentation Hardness of Advanced Ceramics, ASTM International, West Conshohocken, PA, PA, 2015. doi:10.1520/C1327-08.2.

[17] M. Yi, X. Zhang, G. Liu, B. Wang, H. Shao, G. Qiao, Comparative investigation on microstructures and mechanical properties of (TiB + TiC)/Ti-6Al-4V composites from Ti-B4C-C and Ti-TiB2-TiC systems, Mater. Charact. (2018). doi:10.1016/j.matchar.2018.04.010.

[18] Y. Zhang, J. Sun, R. Vilar, Characterization of (TiB + TiC)/TC4 in situ titanium matrix composites prepared by laser direct deposition, J. Mater. Process. Technol. (2011). doi:10.1016/j.jmatprotec.2010.11.009.

[19] M. Das, K. Bhattacharya, S.A. Dittrick, C. Mandal, V.K. Balla, T.S. Sampath Kumar, A. Bandyopadhyay, I. Manna, In situ synthesized TiB-TiN reinforced Ti6Al4V alloy composite coatings: Microstructure, tribological and in-vitro biocompatibility, J. Mech. Behav. Biomed. Mater. 29 (2014) 259–271. doi:10.1016/j.jmbbm.2013.09.006.

[20] J. Wang, L. Li, P. Lin, J. Wang, Effect of TiC particle size on the microstructure and tensile properties of TiCp/Ti6Al4V composites fabricated by laser melting deposition, Opt. Laser Technol. 105 (2018) 195–206. doi:10.1016/j.optlastec.2018.03.009.

[21] Q. An, L.J. Huang, Y. Bao, R. Zhang, S. Jiang, L. Geng, M. Xiao, Dry sliding wear characteristics of in-situ TiBw/Ti6Al4V composites with different network parameters, Tribol. Int. 121 (2018) 252–259. doi:10.1016/j.triboint.2018.01.053.

[22] B. Haldar, S. Karmakar, P. Saha, A.B. Chattopadhyay, In situ multicomponent MMC coating developed on Ti–6Al–4V substrate, Surf. Eng. 30 (2014) 256–262. doi:10.1179/1743294414Y.0000000252.

[23] H. Attar, S. Ehtemam-Haghighi, D. Kent, M.S. Dargusch, Recent developments and opportunities in additive manufacturing of titanium-based matrix composites: A review, Int. J. Mach. Tools Manuf. 133 (2018) 85–102. doi:10.1016/j.ijmachtools.2018.06.003.

[24] D. Gu, G. Meng, C. Li, W. Meiners, R. Poprawe, Selective laser melting of TiC/Ti bulk nanocomposites: Influence of nanoscale reinforcement, Scr. Mater. 67 (2012) 185–188. doi:10.1016/j.scriptamat.2012.04.013.

[25] C. Ma, D. Gu, D. Dai, H. Zhang, H. Zhang, J. Yang, M. Guo, Y. Du, J. Gao, Microstructure evolution and high-temperature oxidation behavior of selective laser melted TiC/TiAl composites, Surf. Coatings Technol. 375 (2019) 534–543. doi:10.1016/j.surfcoat.2019.07.059.

Supplemental Material

Supplementary Table #1: Powder-bed-fusion processing parameters for Ti6Al4V-2.5B$_4$C-2.5BN composites and processing outcome for 5mm tall samples.

Laser Power (W)	Scanning Speed (mm/s)	Hatch Spacing (um)	Layer Thickness (um)	Energy Density (Jmm-3)	Processability
130	1660	70	30	37.3	Crack-Free
130	1840	70	30	33.6	
130	2070	50	30	41.9	
130	2070	60	30	34.9	
123	1980	60	30	34.5	
123	2070	60	30	33	
137	1980	60	30	38.4	
130	1980	70	30	31.3	
130	2070	70	30	29.9	
123	1881	70	30	31.1	
123	1980	70	30	29.6	
123	2070	70	30	28.3	
137	1881	70	30	34.7	
137	1980	70	30	32.9	
137	2070	70	30	31.5	
130	1660	59.5	30	43.9	Minor Cracking
130	1840	59.5	30	39.6	
116	1472	59.5	30	44.1	
116	1660	59.5	30	39.1	
116	1840	59.5	30	35.3	
144	1472	59.5	30	54.8	
144	1660	59.5	30	48.6	
144	1840	59.5	30	43.8	
130	1472	70	30	42.1	
116	1472	70	30	37.5	
116	1660	70	30	33.3	
116	1840	70	30	30	
144	1660	70	30	41.3	
144	1840	70	30	37.3	
130	1980	50	30	43.8	
123	1980	50	30	41.4	
123	2070	50	30	39.6	
137	2070	50	30	44.1	
130	1881	60	30	38.4	
130	1980	60	30	36.5	
123	1881	60	30	36.3	
137	2070	60	30	36.8	
130	1881	70	30	32.9	

130	1472	59.5	30	49.5	Full Cracking
144	1472	70	30	46.6	
144	1120	59.5	30	72	
144	1360	59.5	30	59.3	
144	1600	59.5	30	50.4	
158	1120	59.5	30	79	
158	1360	59.5	30	65.1	
158	1600	59.5	30	55.3	
172	1120	59.5	30	86	
172	1360	59.5	30	70.9	
172	1600	59.5	30	60.2	
130	1881	50	30	46.1	
123	1881	50	30	43.6	
137	1881	50	30	48.6	
137	1980	50	30	46.1	
137	1881	60	30	40.5	

Supplementary Table #2: Powder-bed-fusion processing parameters for Ti6Al4V-1.25B_4C-1.25BN composites and processing outcome for 5mm tall samples.

Laser Power (W)	Scanning Speed (mm/s)	Hatch Spacing (um)	Layer Thickness (um)	Energy Density (Jmm-3)	Processability
103	2070	50	30	33.2	Crack-Free
103	2277	50	30	30.2	
95	2505	50	30	25.3	
103	2070	60	30	27.6	
103	2277	60	30	25.1	
103	2070	70	30	23.7	
113	2505	70	30	21.5	
123	1980	60	30	34.5	Minor Cracking
130	2070	50	30	41.9	
137	2070	70	30	31.5	
130	2070	70	30	29.9	
123	1980	70	30	29.6	
123	1980	50	30	41.4	
113	2070	50	30	36.4	
113	2277	50	30	33.1	
113	2505	50	30	30.1	
123	2070	50	30	39.6	
123	2277	50	30	36	

123	2505	50	30	32.7	
113	2505	60	30	25.1	
123	2505	60	30	27.3	
113	2070	70	30	26	
158	1120	60	30	79	Full Cracking
158	1360	60	30	65.1	
172	1120	60	30	86	
144	1120	60	30	72	
144	1360	60	30	59.3	
172	1360	60	30	70.9	
116	1472	60	30	44.1	
116	1660	60	30	39.1	
116	1840	60	30	35.3	
116	1472	70	30	37.5	
144	1472	60	30	54.8	
137	2070	50	30	44.1	
144	1660	60	30	48.6	
144	1840	60	30	43.8	
130	1472	70	30	42.1	
116	1472	70	30	37.5	
158	1600	60	30	55.3	
172	1600	60	30	60.2	
130	1472	60	30	49.5	
144	1600	60	30	50.4	
130	1881	60	30	38.4	
103	2505	60	30	22.8	
113	2070	60	30	30.3	
113	2277	60	30	27.6	
123	2070	60	30	33	
123	2277	60	30	30	
103	2277	70	30	21.5	
113	2277	70	30	23.6	
123	2070	70	30	28.3	
123	2277	70	30	25.7	
23	2505	70	30	23.4	